Title:

Discretely Assembled Mechanical Metamaterials

Authors:
Benjamin Jenett[1*], Christopher Cameron[2], Filippos Tourlomousis[1], Alfonso Parra Rubio[1], Megan Ochalek[1], Neil Gershenfeld[1]
Affiliations:
[1]Center for Bits and Atoms, Massachusetts Institute of Technology, Cambridge, MA
[2]U.S. Army Research Laboratory, Aberdeen Proving Ground, MD
**corresponding author* bej@mit.edu

Abstract:
Mechanical metamaterials offer novel properties based on local control of cell geometry and their global configuration into structures and mechanisms. Historically, these have been made as continuous, monolithic structures with additive manufacturing, which affords high resolution and throughput, but is inherently limited by process and machine constraints. To address this issue, we present a construction system for mechanical metamaterials based on discrete assembly of a finite set of parts, which can be spatially composed for a range of properties such as rigidity, compliance, chirality, and auxetic behavior. This system achieves desired continuum properties through design of the parts such that global behavior is governed by local mechanisms. We describe the design methodology, production process, numerical modeling, and experimental characterization of metamaterial behaviors. This approach benefits from incremental assembly, which eliminates scale limitations, best-practice manufacturing for reliable, low-cost part production, and interchangeability through a consistent assembly process across part types.

MAIN TEXT

Introduction

The notion of rationally designing a material from the micro to the macro scale has been a longstanding goal with broad engineering applications. By controlling local cell properties and their global spatial distribution and arrangement, metamaterials with novel behavior can be achieved. The foundation for mechanical metamaterials comes from the study of cellular solids (*1*), where natural materials such as wood and bone (*2*), or synthetic materials such as stochastic foams, are understood as a network of closed or open cells (*3*). In the latter case, edges form a network of beams, and based on the connectivity of these beams and their base material, macroscopic behaviors can be predicted analytically (*4*). It was from this insight that the field of architected materials formed, enabling design of periodic structures with tailorable properties such as improved stiffness over foams at similar density due to higher degrees of connectivity (*5*).

Advances in digital fabrication, specifically, additive manufacturing, have enabled these complex designs to be realized. Seminal work demonstrated stiff, ultralight lattice materials (*6*), and has since been improved, resulting in mechanical metamaterials with superior stiffness and strength at ultralight densities (*7*) with multiscale hierarchy (*8*). Benefits of nanoscale features further expand the exotic property parameter space (*9*) and architectures featuring closed-cell plates have shown potential for approaching the theoretical limit for elastic material performance (*10*). Other designs seek to utilize compliance, which can be attained through internal geometric mechanisms (*11*), or through base materials capable of large strain (*12*). Internal architectures can be designed to transmit or respond to load in other non-standard ways. Auxetic metamaterials exhibit zero or negative Poisson's ratio (*13*). Internal, re-entrant architectures produce contraction perpendicular to compressive loading, and expansion perpendicular to tensile loading, counter to traditional continuum material behavior (*14*). Chiral metamaterials exhibit handedness based on asymmetric unit cell geometry. These designs produce out of plane deformations, such as twist, in response to in plane loading (*15*).

Nearly all of the aforementioned mechanical metamaterials are made with some form of additive manufacturing, most of which are summarized in (*16*). These processes vary widely in terms of cost, precision, throughput, and material compatibility. The lower end of the cost spectrum, such as fused deposition modeling (FDM), also tends to have lower performance. Limits of thermoplastic extrusion include layer-based anisotropy (*17*) and errors resulting from build angles for complex 3D geometry (*18*). Higher performance, and higher cost, processes such as selective laser melting (SLM) utilize materials such as stainless steel, but require non-trivial setup for particulate containment, and can suffer from layer-based anisotropy, thermal warping, and geometry irregularity (*19*). Some of the highest performance multi-scale metal microlattice production techniques based on lithographic and plating processes are well-studied and repeatable but are also highly specialized and labor-, time-, and cost-intensive. Polymerization, curing, plating, milling, and etching can require up to 24 hours from start to finish for sample preparation (*6*). Large area projection microstereolithography (LAPμSL) is capable of producing lattices with μm (10^{-6} m) scale features on centimeter (10^{-2} m) scale parts (*8*) with significantly improved throughput, but extension to macro-scale (>1m) structures remains out of reach, due to practical limitations in scaling these processes and their associated machines.

The largest structure that can be printed with any given process is typically limited by the build volume of the machine. Therefore, significant effort is focused on scaling up the machines. Meter-scale FDM platforms (*20*) and larger cementitious deposition machines (*21*) have been demonstrated, and coordinated mobile robots are proposed to achieve arbitrarily large work areas (*22*). However, there is a tradeoff between precision, scale, and cost. Commercially available two-photon polymerization machines have resolution on the order of 1 μm (10^{-6} m), build size on the order of 100mm (10^{-1} m), and cost on the order of 10^6 \$/machine (*23*). Macro-scale FDM machines boast build sizes of 10^1 m (*24*) but are unlikely to have better than mm (10^{-3} m) resolution. Thus, roughly the same dynamic range (scale/resolution) is offered, but with costs approaching 10^7 \$/machine, we see a possible super-linear cost-based scaling of achievable dynamic range. Building large, precise machines is expensive, and due to the inherent coupling of machine performance, size, and cost, there are significant challenges for realizing macro-scale (>1m) mechanical metamaterials with high quality and low cost.

An alternative approach to producing mechanical metamaterials seeks to decouple these aspects, and in doing so overcome machine-based limitations. Based on reversible assembly of discrete, modular components, this method utilizes mechanical connections to build larger, functional metamaterials and structures out of smaller, mass-producible parts. The first demonstration of this approach utilized custom wound, centimeter-scale, carbon fiber reinforced polymer (CFRP) components (*25*), resulting in an ultralight density lattice with improved elastic stiffness performance over then state of the art metallic microlattice (*6*), due to the high modulus constituent material. Following this, larger scale, octahedral voxel (volumetric pixel) building block units were made using commercial off the shelf (COTS) high modulus, unidirectional pultruded CFRP tubes connected with injection molded glass fiber reinforced polymer (GFRP) nodes, resulting in a macro-scale (>1m), high performance, reconfigurable structure system (*26*). Following this, entire voxel units were made with injection molding of GFRP, yielding the first truly mass-producible discrete lattice material system with low cost, best-practice repeatability, and high performance (*27*). Discrete assembly offers scalability and functionality not achievable with traditional methods due to process and machine limitations.

In this paper, we present a construction system for mechanical metamaterials based on discrete assembly of a finite set of modular, mass produced parts. We demonstrate experimentally the desired metamaterial property for each part type, and combined with numerical modeling results, display other novel, unexpected properties. A modular construction scheme enables a range of mechanical metamaterial properties to be achieved, including rigid, compliant, auxetic and chiral, all of which are assembled with a consistent process across part types, thereby expanding the functionality and accessibility of this approach. The incremental nature of discrete assembly enables mechanical metamaterials to be produced efficiently and at low cost, beyond the scale of the 3D printer.

Results

Continuum behavior from discrete parts

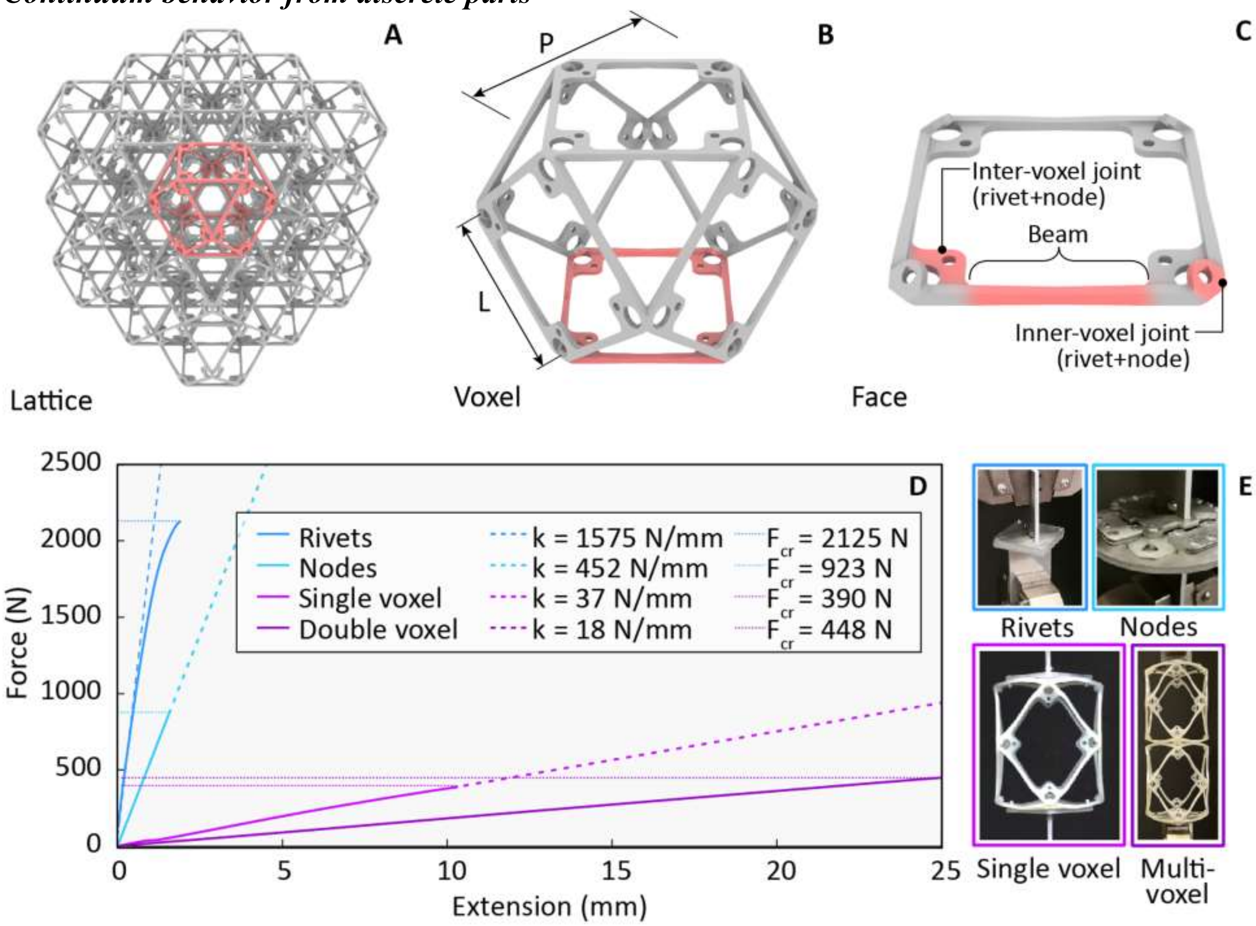

Figure 1: Discrete mechanical metamaterial subsystem description and characterization. *A) 3x3x3 lattice consists of 27 individual voxels, B) Voxels consist of six individual faces, C) Faces consist of beams and joints, D) Experimental results for subsystem characterization, where we see joints (rivets + nodes) are individually stiffer and stronger than voxels, which are governed by beam properties E) Subsystem testing setups.*

First, we present the discrete material construction system and show how continuum behavior is achieved through design of the parts and their relative structural performance. Parts are designed to have their local beam properties govern global lattice behavior, resulting in an effective bulk material that behaves as if it were produced monolithically.

A lattice, or a mechanical metamaterial consisting of a periodic network of interconnected beams, can be described, and its performance predicted, analytically. We can describe lattices as stretch- or bending-dominated, based on how they resolve external forces as a function of their internal beam connectivity, which corresponds to Maxwell's frame rigidity criteria extended to 3D (*5*). Stretch-dominated lattices, such as the octet, have higher connectivity ($Z = 12$) and higher stiffness to weight than bending-dominated lattices, such as the kelvin, which have lower connectivity ($Z = 4$) (*7*). In this work we use the cuboctahedra lattice (referred to as Cuboct) geometry, which is uniquely positioned between low and high connectivity ($Z = 8$) yet has been shown to have stretch-dominated behavior, in both microlattice implementation (*28*) and as discretely assembled vertex connected octahedra (*27*).

In Figure 1A-C, we show a new decomposition using face-connected cuboctahedra voxels which produces the same lattice geometry but has additional benefits to be discussed herein. Voxels are discretized into faces, which consist of beams and joints. There are two types of joints: inner-voxel joints are the points at which 6 separate faces are joined to form a voxel, and inter-voxel joints provide the vertex to vertex connections between neighboring voxels along a single face. A joint consists of nodes, which are the geometric features on the part providing the fastening area, and the fasteners, which are mechanical connectors. Based on the material and geometric properties of each subsystem, local properties can be controlled to ensure proper global, continuum behavior. In this case, our lattice should behave as an interconnected network of beams. Therefore, we wish to design joints to possess significantly higher effective stiffness and strength than the beams they connect. In this way, the global effective stiffness and strength of the lattice are governed by those subsystems with the lowest relative value.

Following as-molded material characterization to calibrate analytical and numerical models (Figure S1), subsystems were then characterized in tests designed to isolate the critical performance aspects for proper system behavior. Rivets, inter-voxel nodes, individual voxels (consisting of beams and inner-voxel joints), and multi-voxel assemblies were tested. The specific goal is to quantify the degree to which voxel and multi-voxel behavior is governed by stiffness and strength properties of the beams, rather than the joints. Experimental results are shown in Figure 1D, with axial stiffness and critical load values noted.

Since each subsystem effectively acts across the same cross section (a single voxel), we can directly compare their yield strength using their observed failure loads. We see the inter-voxel node and fastener yield strengths are roughly two and four times the voxel yield strength, respectively. For axial stiffness, we treat single and multi-voxel tests as effective springs in series. A single voxel then consists of five effective springs in series: top fasteners, top nodes, voxel, bottom nodes, and bottom fasteners. For springs in series, the equivalent axial stiffness is the reciprocal of the sum of the individual spring reciprocals:

$$\frac{1}{k_{eq}} = \sum_{i=1}^{n} \frac{1}{k_i}$$

$$k_1 \ll k_{i>1}$$

$$k_{eq} \approx k_1$$

For large k_i and small k_1, we see that k_{eq} equals k_1, indicating that the governing value is the lower spring stiffness. Using measured values for fasteners, nodes, and voxels, we see the experimental value for the two-voxel assembly agrees with this analytical description, and that both effective stiffness and strength are governed by voxel, and thus beam, properties. Additional details on the joint load paths and hysteresis effects are presented in the supplementary material. Under cycling the hysteresis rapidly decreased to a stable value, which for the stiffest lattice (cuboctahedral) was approximately twice the base material, corresponding to matching the hysteresis of a rigid rubber at a fraction of a percent of the density (*53, 54*). This can be further reduced with preloaded joints (*27*).

Part types

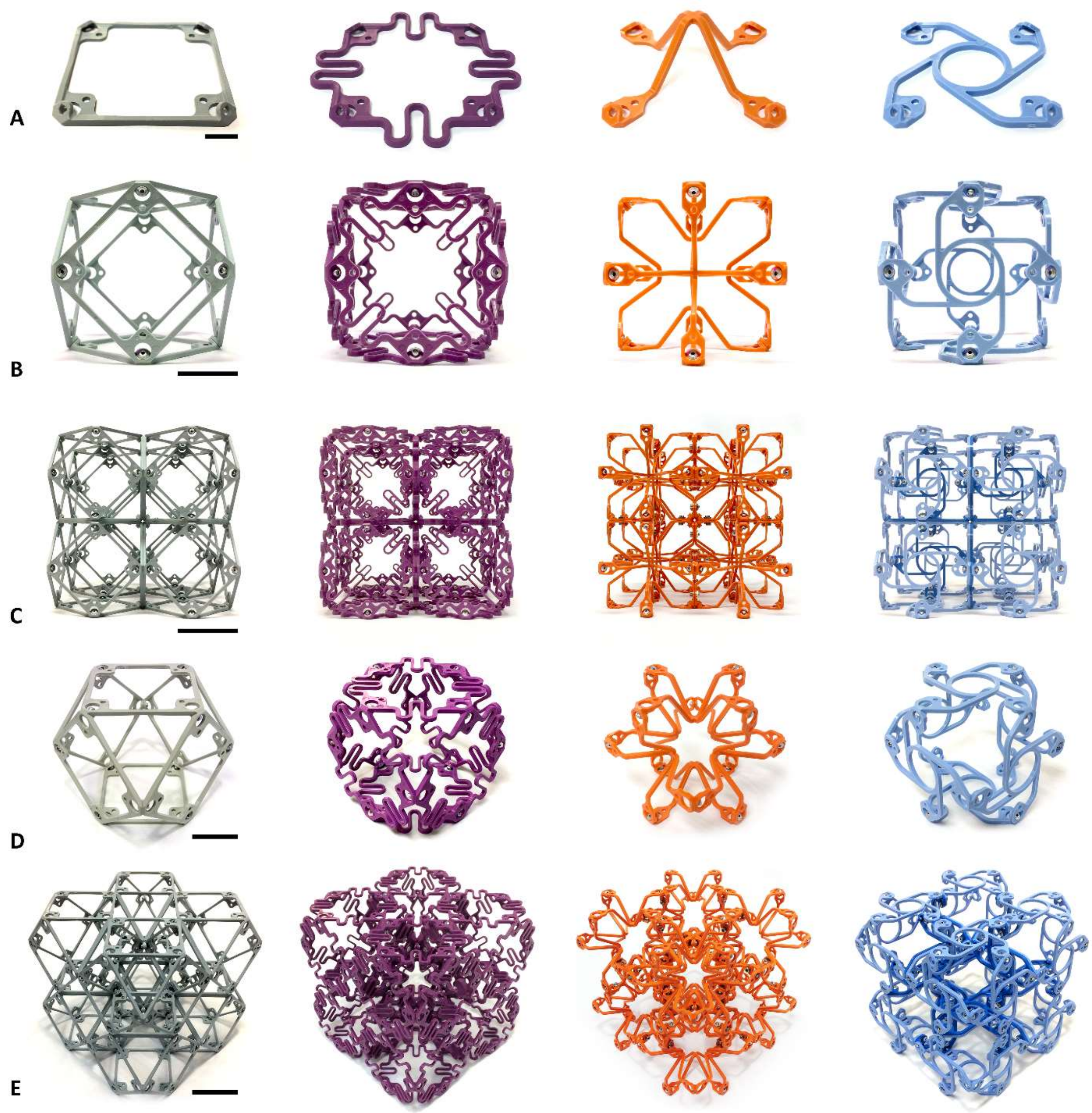

Figure 2: Four types of discretely assembled mechanical metamaterials. *Left to right: rigid, compliant, auxetic, and chiral. A) As-molded face parts, B) Single voxel, front view, C) 2x2x2 Cube, front view, D) Single voxel, oblique view, E) 2x2x2 oblique view. Scale bars: A) 10mm, B, D) 25mm, C, E) 50mm.*

Using this construction system, we present the discretely assembled mechanical metamaterials consisting of four part types: rigid, compliant, auxetic, and chiral, shown in Figure 2. Six face parts (Figure 2A) are assembled to form voxels (Figure 2B), which are then assembled to form multi-voxel lattices (Figure 2C). Details of the assembly procedure and throughput metrics can be found in Supplementary materials.

Rigid voxels resolve external loading through axial beam tension and compression, resulting in elastic, followed by plastic, buckling of struts. Lattices made with these parts show near-linear scaling of effective modulus, positive Poisson ratio, and yield strength determined by geometric and manufacturing process parameters. Compliant voxels are designed with corrugated flexure beams, a motif found in flexural motion systems (*29*), which resolve axial beam forces through elastic deformation of the planar flexures. Lattices made with these parts show consistent elastomeric behavior at even single voxel resolution and have a near-zero Poisson ratio. Auxetic voxels are designed as intersecting planes of re-entrant mechanisms, which expand and contract laterally under uniaxial tension and compression, respectively. Lattices made with these parts show a negative Poisson ratio through a combined action of pure mechanism and flexural beam bending. Chiral voxels are designed with an asymmetric mechanism which responds to in plane loading by producing either clockwise (CC) or counterclockwise (CCW) rotation. When interconnected in three dimensions, this produces out of plane twist in response to uniaxial tension or compression. By combining CC and CCW parts, internal mechanism frustration can be avoided, enabling improved scalability over prior art. The four lattice types and their behaviors will be described in further detail in the following subsections.

Rigid Lattice Behavior

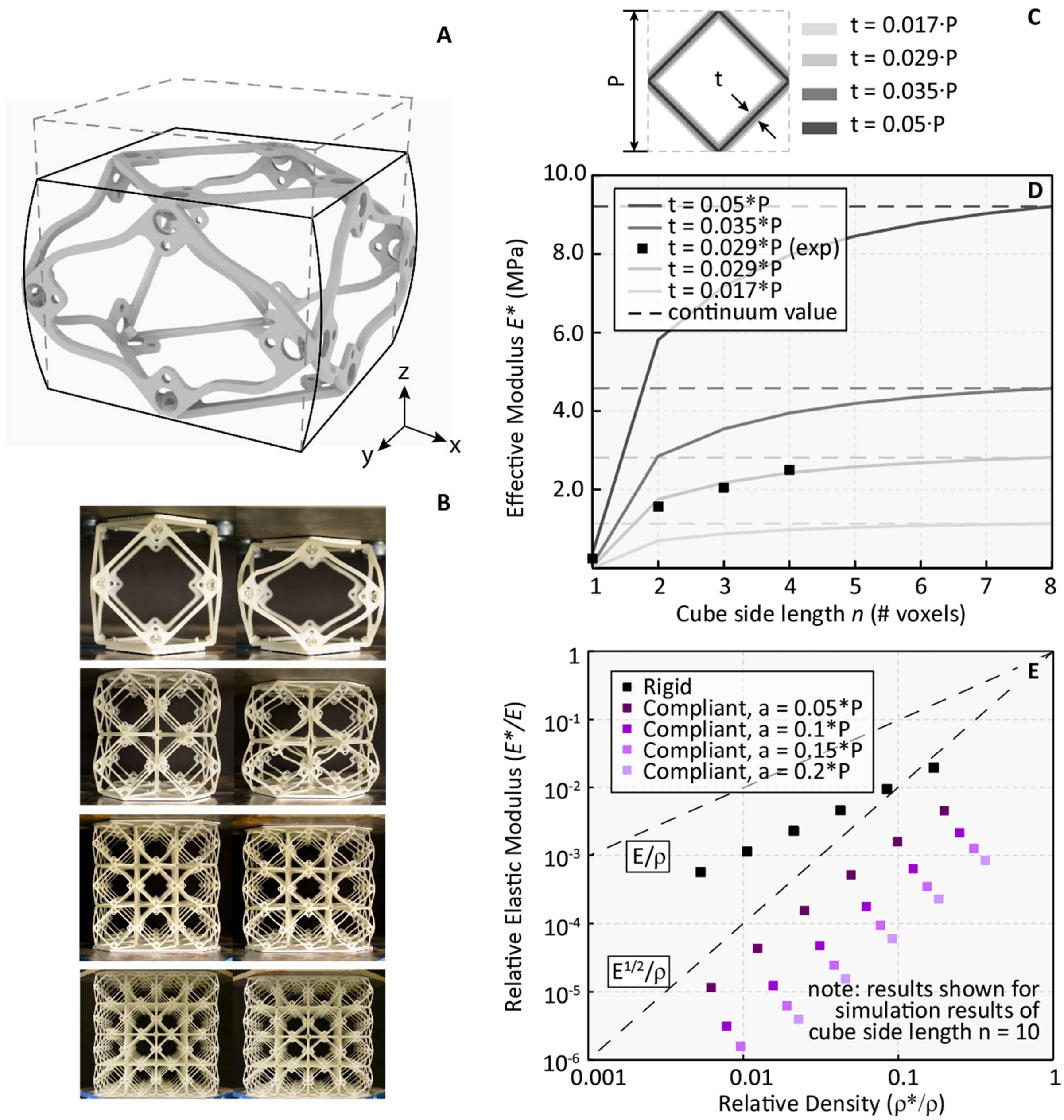

Figure 3: Rigid mechanical metamaterial. *A) Characteristic unit cell voxel demonstrating beam buckling and positive transverse strain in response to compressive load, B) Experimental test setup for* n = 1-4, *undeformed (L), and at initial beam failure (R), C) Geometric parameters for simulations, where beam thickness* t *is a function of lattice pitch* P, *D) Effective stiffness for reduced order beam model simulation and experimental results demonstrating asymptotic behavior approaching continuum value at increasing voxel count E) Reduced order beam model simulation results for rigid and compliant lattice of 10x10x10 cube. Observable are modulus-density scaling values being linear for rigid and near quadratic for compliant.*

The rigid lattice type exhibits relative modulus-density scaling which matches previous results in literature but does so with a novel geometric decomposition. We present experimental and numerical results for the rigid lattice type in Figure 3. The characteristic behavior of a unit cell voxel is shown in Figure 3A. The geometry is isotropic along its primary axes, and it responds to loads through axial beam tension and compression. While individual voxels are dominated by under-constrained, mechanism behavior of the quadrilateral faces, when multiple voxels are joined, there is sufficient connectivity to provide rigidity through triangulation of neighboring voxel faces. As a result, effective modulus increases with increasing cell count, and this value eventually reaches an effective continuum value, as seen in Figure 3D.

Having established that the global behavior is governed by the beam properties, now we can correlate analytical models with experimental results for effective lattice behavior. Here we will look at effective elastic modulus E^* and yield strength σ_y, the former corresponding to the linear portion of the stress strain curve under quasi-static loading, and the latter corresponding to the failure load divided by the specimen cross section area. Stress-strain curves for lattice specimens of cube side voxel count n = 1-4 are shown in Figure S10, where an initial linear elastic regime is followed by a non-linear elastic regime and plastic yield. Using load and displacement data, stress and strain values are calculated based on lattice specimen size. The calculated moduli are shown with numerical results in Figure 3D, in this case using the reduced order beam models as described in *Materials and Methods*. It can be seen that as voxel count n increases, E^* approaches a continuum value depending on the beam thickness, and thus relative density of the lattice. In the case of our built lattice, voxel cubes of side voxel count n = 1-4 have effective moduli relative to the continuum approximation (horizontal line, value for 10x10x10 determined numerically) of 9, 56, 73, and 89%, respectively. Discrepancy between experimental and numerical results are also calculated for specimens n = 1-4 to be 458, 10, 6, and 3%, respectively. This can be attributed to the ratio of internal to external beams increasing as voxel count increases (Figure S7). The internal beams, which are fully constrained and behave as a rigid network, asymptotically govern the effective global behavior.

These predicted effective lattice properties over the range of effective densities are plotted relative to constituent values in Figure 3E. The slope of the curve connecting these points, plotted on a log/log chart, provides the power scaling value, which is used to analytically predict lattice behaviors at the macroscopic scale (*4*). Effective lattice modulus and density are related to constituent material modulus and density by $\frac{E^*}{E} \propto \left(\frac{\rho^*}{\rho}\right)^b$, where b is 1 for stretch dominated lattices and 2 for bending dominated. We find b = 1.01 for our rigid lattice. This scaling value had been shown previously for the monolithic (additively manufactured) cuboctahedron lattice (*28*) and for discretely assembled, vertex connected octahedra (*27*), to which we now add our novel lattice decomposition. It should be noted that these effective values are from numerical simulations, not experiment, though we direct the reader to Figure 3D and Figure 4D for agreement between experimental and numerical results.

Next, we compare experimental yield stress results with analytical predictions of local beam failure based on relative density, as a function of beam thickness t and lattice pitch P. Here, we will use experimental data from the 4x4x4 specimen, as this is closest to demonstrating continuum behavior (effective modulus is 89% predicted continuum value). Based on the load at failure and lattice material and geometry, we can determine a given beam compressive failure load to be around 88N. We determine the analytical critical beam load using either the Euler buckling formula or the Johnson parabola limit, depending on the compression member's slenderness ratio (Figure S5). We determine our beam slenderness ratio to be 29.5, which is over the critical slenderness ratio of 19.7 (see supplementary material for complete calculation), thus we use Euler buckling formula. Because the as-molded material properties vary, we determine the critical load to range from 70 to 108 N, with the mean value of 89 N very closely approximating the experimental value. Thus, there is good correlation between both stiffness and strength based on the design of our discrete lattice material.

Compliant Lattice Behavior

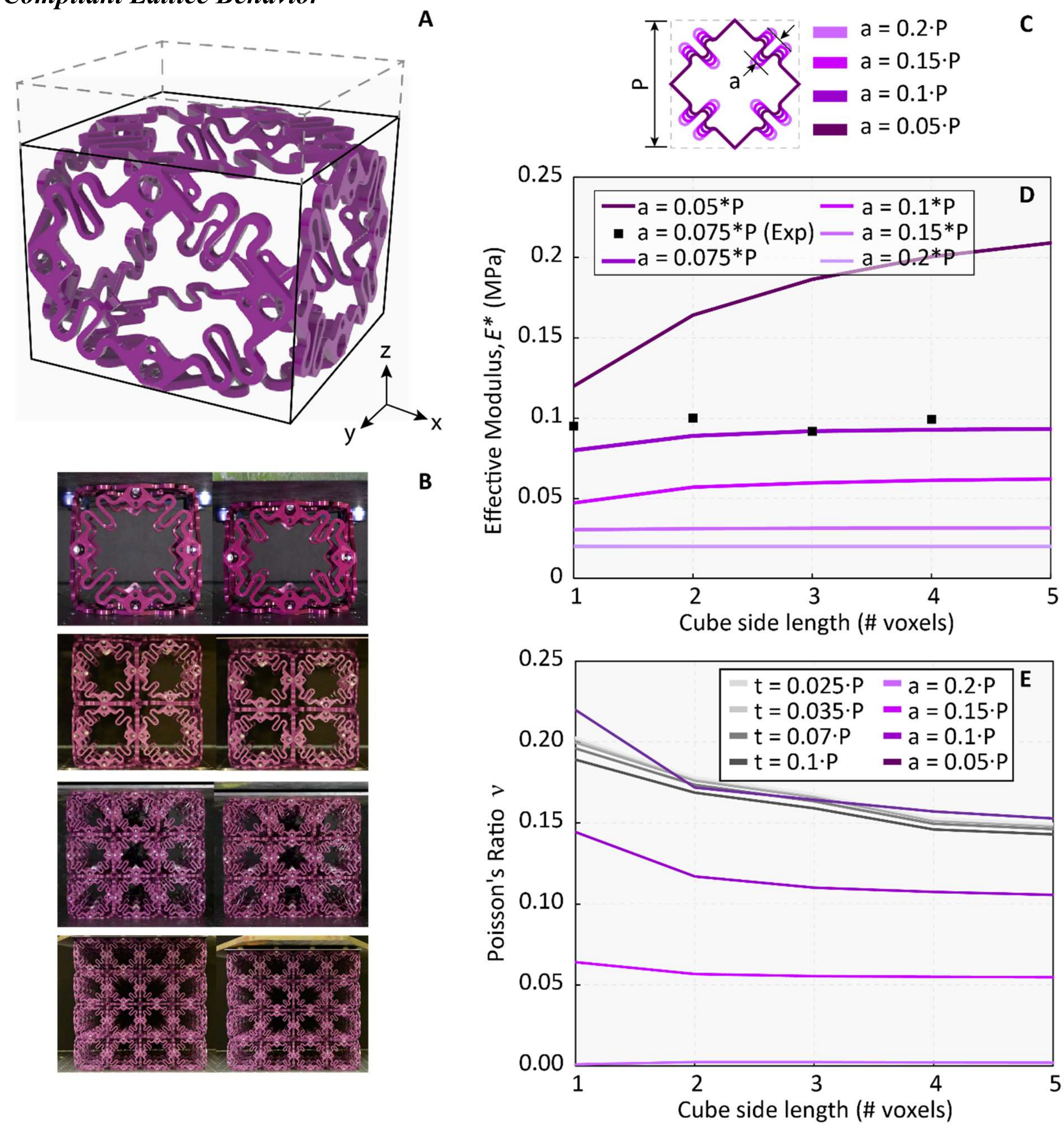

Figure 4: Compliant mechanical metamaterial. *A) Characteristic unit cell voxel demonstrating flexure spring-beam deformation and small transverse strain in response to compressive load, B) Experimental test setup for* n = 1-4, *undeformed (L), and at onset of non-linearity (R), C) Geometric parameters for simulations, where spring-beam amplitude* a *is a function of lattice pitch* P*, D) Effective stiffness simulation and experimental results, which show near continuum value at low voxel count for all but the smallest spring-beam amplitude designs, E) Simulation results for effective Poisson's ratio for rigid and compliant lattice, with large spring-beam amplitudes having a value of near zero.*

The compliant lattice type exhibits quadratic scaling for effective stiffness, as well as consistency across voxel counts regarding continuum behavior and elastic limit values. We present experimental and numerical results for the compliant lattice type in Figure 4. The characteristic behavior of a unit cell voxel is shown in Figure 4A. While the load paths are topologically the same as the rigid voxel, as this is a function of lattice connectivity, the mechanism through which beams resolve these loads is different. Here, the planar-spring beams deform in combined axial and in-plane bending, as a controllable property of the compliant features we design. This produces several unique behaviors in this lattice type.

First, we can see from the experimental stress-strain curves that for similar strains, the compliant lattice shows linear elastic behavior up until the elastic limit (Figure S10-B). The stress at which this transition occurs is consistent across voxel counts, from $n = 1$ to $n = 4$. Second, the effective modulus is also consistent across voxel counts. This is confirmed by simulations using reduced order beam models, as shown in Figure 4D. Given the large range of linear to non-linear and individual to continuum behavior seen in the rigid lattice, the compliant lattice is markedly different in its consistency. This behavior is attributable to the spring-like behavior of the beams, a similar observation to analytical models for stochastic foams (*30*). As cube specimen side length voxel count increases, so do the number of springs acting in parallel, which produces an effective spring stiffness $K_{eff} = K_1 + K_2 + K_n \ldots$. But as spring count increases, so does effective area, both proportional to side length squared. Thus, a single voxel has the same effective modulus as a 4x4x4 or an $n \times n \times n$ cube. This effect is reduced as beam-spring amplitude a goes to zero, meaning it shows more asymptotic behavior similar to the rigid cuboct lattice.

Another property observed experimentally, and confirmed numerically, is a low, near-zero, Poisson's ratio. Figure 4E shows the simulated effective Poisson's ratios for the compliant and rigid voxel. At the largest compliant amplitude, we see a value of near zero. As the amplitude a of the compliant spring feature goes to zero, the Poisson's ratio converges to around 0.15, which is the effective value for the entire parameter range of the rigid lattice.

Finally, this lattice shows near quadratic stiffness scaling, in contrast to the near linear scaling shown by the rigid lattice, while having the same base lattice topology and connectivity as the rigid version (Figure 3E)—meaning it has bending-dominated behavior with a stretch dominated lattice geometry. The range of spring amplitudes as a function of lattice pitch P shown in Figure 3E are $a = 0.05$, 0.1, 0.15, and 0.2, and these have scaling values of $b = 1.72$, 1.89, 1.93, and 1.95, respectively. This is attributable to the localized behavior of the spring-like beams. Whereas in the rigid lattice vertically oriented beams in compression are offset by horizontally oriented beams in tension, resulting in stretch dominated behavior, here global strain is a function of local spring-beam strain, which does not produce significant reactions at beam ends opposite an external load.

Auxetic Lattice Behavior

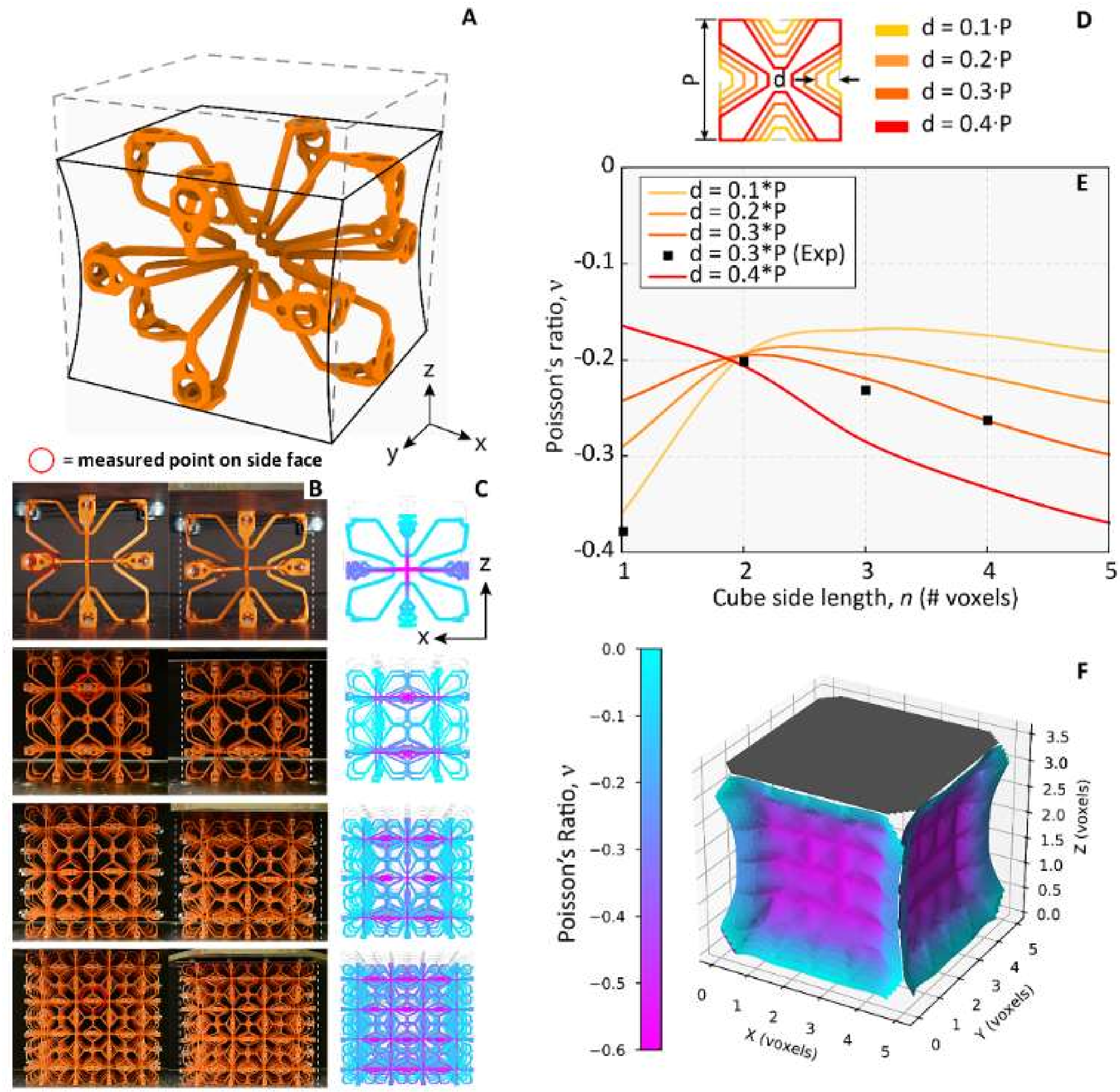

Figure 5: Auxetic mechanical metamaterial. *A) Characteristic unit cell voxel demonstrating reentrant mechanism action resulting in negative transverse strain in response to compressive load, B) Experimental test setup for* n = 1-4, *undeformed (L), and deformed to 0.2 strain (R), with measured points on side faces circled in red, C) Reduced order beam model simulation results recreating experiments, with out of plane reentrant behavior highlighted, D) Geometric parameters for simulations, where reentrant distance* d *is a function of lattice pitch* P*, E) Effective Poisson's ratio simulation and experimental results, F) 3D contour plot demonstrating effect of boundary conditions resulting in near zero Poisson's ratio at edges.*

The goal of the auxetic lattice type is to exhibit a controllable negative Poisson's ratio. We present experimental and numerical results for the auxetic lattice type in Figure 5. The characteristic behavior of a unit cell voxel is shown in Figure 5A. Due to the internal architecture, which consists of interconnected, re-entrant mechanisms seen elsewhere in literature (*14*), the cell responds to axial strain with a similarly signed transverse strain, resulting in a negative Poisson's ratio *v*, where $\nu = -\frac{\epsilon_{trans}}{\epsilon_{axial}}$. This value can be controlled based on the re-entrant distance d as a function of lattice pitch P, as shown in Figure 5D.

Experimental results are shown in Figure 5B. Lattice specimens are cubes of voxel width n = 1-4. Specimens were compressed to identical strain values ($\epsilon_{axial} = 0.2$), and transverse strain was measured by visually tracking points using fiducials mounted to the nodes along transverse faces (*yz* plane) parallel to the camera. Experimental data can be found in Figure S10-C. These points are slightly obscured due to reduced reentrant behavior at the edges of the lattice. In Figure 5C, we show contour plots element translation in the *y* direction, which is out of plane and normal to the camera view. While this behavior is generally isotropic, it should be noted that the effect of the internal mechanisms is reduced at the corners/edges of the cube specimen, as shown in Figure 5F. The median effective strain values are plotted in Figure 5E over the range of parameters shown in Figure 5D. The median was chosen to reduce the influence of the boundary conditions where $\nu \approx 0$. The experimental Poisson's ratios, indicated as black squares, were measured using fiducial targets and motion tracking at the points indicated in Figure 5B.

There are two main insights from this study. First is that the effective metamaterial behavior approaches a nominal continuum value as cube side length of voxel count n increases. For any re-entrant distance, this behavior can be attributed to the increase of internal mechanism architecture relative to boundary conditions. Boundary conditions increase as a function of surface area proportional to n^2, while internal mechanism architecture increases as a function of specimen volume proportional to n^3. For lower values of d, the single voxel demonstrates lower values for Poisson's ratio (increased auxetic behavior) compared to multi-voxel specimens, but this is strongly influenced by boundary conditions, and can be considered an outlier.

The second insight is that the effective Poisson's ratio decreases (becomes more negative) as re-entrant distance d is increased, for voxel specimens larger than $n = 1$. This can be understood by considering the continuous beams of the re-entrant faces as a pseudo rigid body model (PRBM), where continuous flexural mechanisms are discretized as effectively rigid links connected by planar joints with torsional stiffness (ie: a spring) (*31*). As d decreases, so does link length, causing less clearly defined boundaries between the rigid link and compliant spring joint (see supplementary material for further analysis). As a result, the rigid link behavior begins to dominate, causing higher overall effective stiffness and lower compliance, thus reducing the re-entrant mechanism efficacy.

Chiral Lattice Behavior

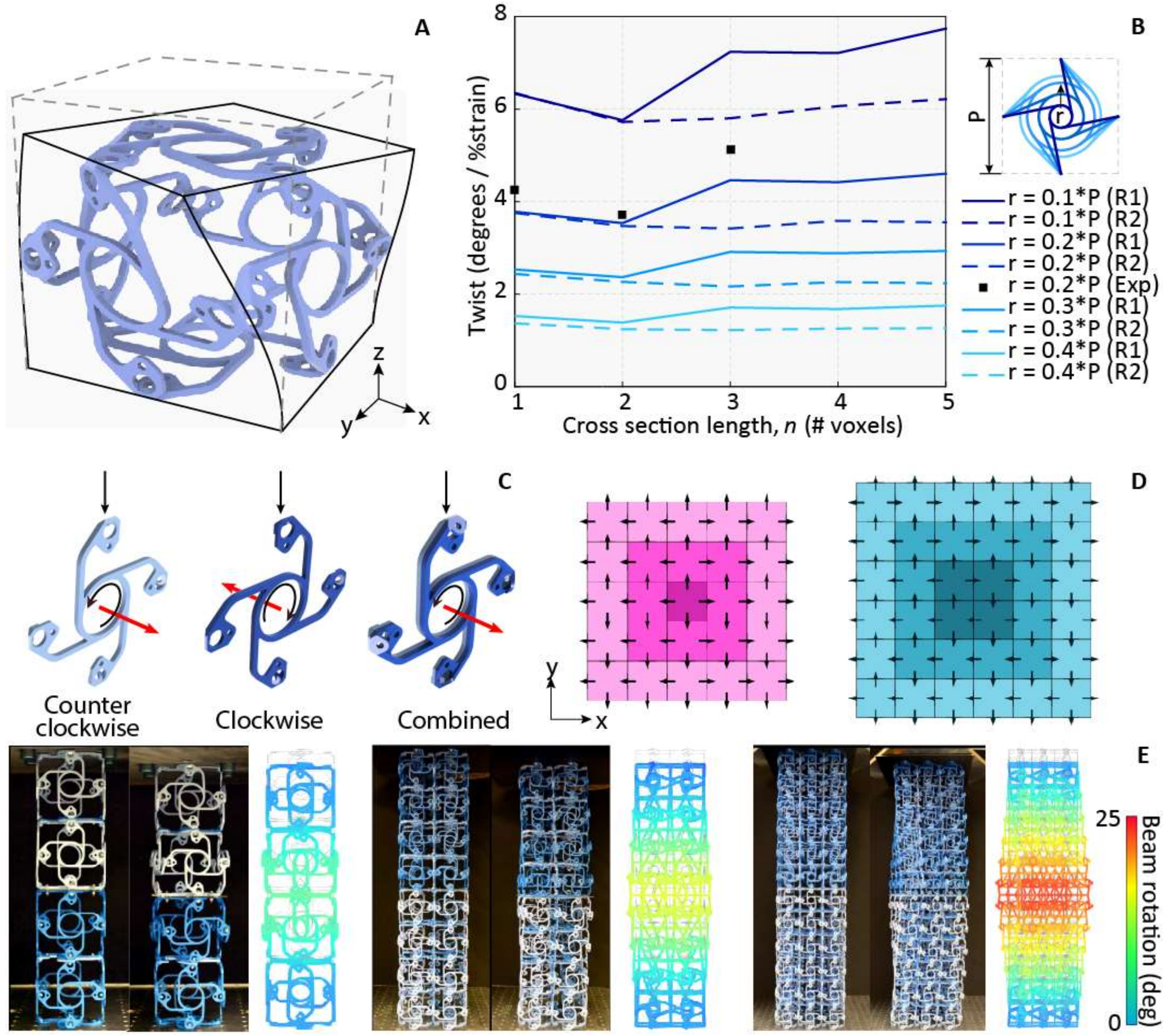

Figure 6: Chiral mechanical metamaterial. *A) Characteristic unit cell voxel demonstrating out of plane coordinated rotation in response to compressive load, B) Simulation and experimental results for odd and even column cross sections in combination with design rules 1 and 2, C) Two chiral part types allow internal frustration to be avoided, thus enabling scalable chiral architecture, D) Design rules 1 (L) and 2 (R), which emerge from odd and even columns, respectively, E) Experimental and reduced order beam model simulation results of* n = *1, 2, and 3, showing total twist increases as column voxel width increases, but normalized twist per strain is lower for* n = 2.

The chiral lattice type exhibits scalable twisting behavior, which is attributable to having two chiral part types, and developing a construction logic to avoid internal frustrations. We present experimental and numerical results for the chiral lattice type in Figure 6. The characteristic behavior of a unit cell voxel is shown in Figure 6A. Based on the chirality orientation, the cell will respond to an axial strain with a macroscopic twisting in either the CW or CCW direction, in the plane normal to the direction of loading (ie: loading in z direction results in twisting in xy plane). The effective chirality can be measured as degrees twist per unit strain.

Experimental results are shown next to their numerical simulations in Figure 6E. Lattice specimens are designed as columns with 1:4 width to height ratio, similar to (*15*). The top half is CCW chiral lattice and the bottom half is CW chiral lattice. This produces the largest net twist at the rigid interface between the two halves and allows fixed boundary conditions at the top and bottom. Chiral columns of 1x1x4, 2x2x8, and 3x3x12 were tested in compression to identical strain values ($\epsilon_{axial} = 0.05$), and twist was measured by tracking a single point at the center of the lattice. Experimental results are shown in Figure S10-D. Surprisingly, the 1x1x4 shows larger values for twist than the 2x2x8. This is attributable to internal architecture, which is also the cause of the scalable twisting found over a range of beam sizes.

Experimental values for twist per strain are shown next to reduced order beam model simulation results in Figure 6B, over a range of values for radius r of the face part as a function of lattice pitch P, with increasing column voxel width n. We observe an increased twist per axial strain for smaller values of r. This is attributable to the direct relationship between strain and twist as a function of the rotational mechanism. If we assume a unit strain is translated into an arc length s, then the rotation angle θ increases as circle radius r goes to zero, given . However, given a nominal beam thickness t, there is a limit to how small r can become before the mechanism becomes ineffective. See supplementary material for further analysis.

There are several key takeaways from this. First, we see that performance does not decrease monotonically with increasing voxel count n, but rather stabilizes to a continuum value. This is in contrast to comparable results in literature (*15*), and can be explained by looking more closely at the combination of CW and CCW part types. Done properly, internal frustrations—when CW and CCW faces are joined they essentially cancel each other's twist, resulting in zero twist per strain—can be avoided, as shown in (*32*) by using voids. In our case, we get improved twist performance by designing the internal architecture according to rules chosen to avoid frustration. This means that voxel types are directionally anisotropic, in contrast to the previous three lattice types, and further are spatially programmed to produce desired global effective behavior. Strategies for this spatial programming are shown in Figure 6C. On the left, we show a beam with odd number voxel widths. Here, design rule #1 is to orient the net face chirality (represented as arrows) away from the column interior. The experimental lattices for n=1 and n=3 widths were built using rule #1. Design rule #2 was developed starting from n=2, where the orientation of interior faces is ambiguous when following rule #1. Rule #2 introduces continuous, clockwise circumferential orientation of the interior chiral faces and was used in construction of the n=2 experimental articles. Both rules are hierarchical, e.g. a rule #1 5x5 column contains a 3x3 and 1x1 column in its interior as shown in Figure 6C. Simulations were performed for all column widths using both rules and show decreased twist response for rule #2, in agreement with experimental measurements. These rules were determined empirically and are not considered exhaustive but indicate the importance of rational design in this lattice type.

Discussion

In this paper, we presented a method for producing large scale mechanical metamaterials through discrete assembly of modular, mass-produced parts. We showed that bulk, continuum behavior can be achieved through design of the parts and connections, ensuring global behaviors are governed by local properties. We presented a finite set of part types which exhibit a diverse range of behaviors. Rigid lattice types show linear stiffness-to-density scaling with predictable failure modes. Compliant lattice types show quadratic stiffness-to-density scaling, as well as unique bulk behavior at low cell count, such as near-zero Poisson's ratio. Auxetic lattice types show controllable, isotropic negative Poisson's ratio. Chiral lattice types show scalable transverse twist in response to axial strain, which is a result of two part types being used to prevent internal architectural frustration. All four part types showed good agreement with numerical results, and their behavior is predictable through analytical means. All lattice types are made the same way: parts are injection molded and assembled to make voxels, and voxels are similarly joined to build lattices. This is a low cost, highly repeatable process that promises to enable mechanical metamaterials at macro scales (Figure S13).

There are several advantages resulting from discrete assembly which make it stand out from existing fabrication methods currently available for producing metamaterials, which include increased functionality, repairability, reconfigurability, and scalability. While this work presented mechanical metamaterials, discretely assembled electromagnetic materials have been previously demonstrated. Passive and conductive parts have been assembled into heterogeneous, functioning 3D circuitry (*33*), and rigid, flexural, and actuated building block parts were used to assemble modular microrobots (*34*). These are millimeter to centimeter scale parts, and the extension of this approach to larger scales is expected to enable novel, mesoscale cellular robots. Due to the discrete nature of the construction, damaged or broken parts can be removed and replaced. This was demonstrated in prior work (*27*), where lattice specimens were tested to initial failure (plastic beam buckling and rupture), then unloaded, the damaged voxel unit was removed and replaced, then the specimen was tested again. Repaired specimens showed only 1.5% loss of effective stiffness and 5% loss of effective strength. Quasi-static reconfigurability was demonstrated through the assembly, disassembly, and reuse of macro-scale (225mm pitch) octahedral voxels (*26*). In that case, over 125 voxels were used to build a 5m bridge capable of holding several hundred kilograms, then these were reconfigured into a boat, then these were again reconfigured into a shelter. Scalability has been demonstrated in prior work, where over 4,000 injection molded octahedral voxel units were assembled into a 4.25m wingspan ultralight lattice aerostructure (*35*). The parts were manually assembled, with a mass and volumetric throughput that was competitive with typical mesoscale additive processes such as SLM and FDM. The machine cost and process challenges associated with making such a lattice structure with either of those methods highlights the benefits of this approach. Scaling to part counts above 10^3 will benefit greatly from assembly automation. Stationary gantry platforms have been fitted with end effectors for voxel transport and bolting operations (*46*), and mobile robots have been implemented to perform similar operations while locomoting on the lattice as they construct it (*47*). Stationary systems promise high throughput for a bounded work envelope, while mobile robots can be parallelized and require no global positioning due to local alignment features, offering benefits of autonomy and reliability. Automation will be critical for producing these metamaterials and structures in large quantities envisioned for commercial applications.

Injection molding as used here offers low cost and high repeatability, but it immediately limits which constituent materials can be used. Sheets of material could be used with subtractive processes such as milling, laser or waterjet cutting to make voxel face parts, though redesign of the joints would be needed. Prior work has shown successful lattice production this way, using a snap fit connection which needs a final adhesive or thermal bonding step to remove the final degrees of freedom at the joints (*42-45)*. Natural materials such as wood can be used this way, and in the future moldable bio-based resins with natural fibers are expected to be commercially available. Looking at scaling down our process, there are some practical limitations to both the part production and the assembly. Scaling down the parts by an order of magnitude (from 75mm cell pitch to 7.5mm cell pitch) should be possible based on current best practice micro-injection molding and existence of commercially available micro-fasteners (see supplementary material for details). Scaling down further (sub-mm cell pitch) would require novel part production and joining methods, suggesting this may be a regime where conventional additive processes are preferable. Rather than focus on absolute length scale, for our metamaterials we are concerned with the ratio of cell size to smallest characteristic system size. Given the quasi-static loading in our case, where the wavelength $2\pi/k$ goes to infinity (*39*), we easily achieve sub-wavelength cell size, while also demonstrating effective continuum properties as a function of local cellular architecture. Thus, the ability to compose macroscopic metamaterials blurs the boundaries between material and structure.

Finally, we limited our study to a set of four distinct behaviors, shown as separate homogeneous lattices. Comparable demonstrations of these properties exist in prior art, but each has typically entailed dedicated development, whereas here we show a single scalable system capable of achieving this range with a consistent production process based on discrete assembly. Due to this, heterogeneous lattices can be made with this approach just as easily. Heterogeneous metamaterials have been shown to offer exponential combinatorial possibilities (*48*), as well as the ability to realize any arbitrary elasticity tensor (*49*). Further, the design of novel part geometries with blends of behavior is a promising next step for use in assembling spatially graded heterogeneous structures, which is one of the main benefits sought through additive processes (*51*) to achieve functionality seen in natural systems (*52*). By offering a simple yet diverse set of parts unified with a consistent assembly method, this work represents a significant step in lowering the barrier for entry to realizing the promise of metamaterials, especially for macro-scale applications. Combined with hierarchical design tools and assembly automation, we foresee this research enabling emerging fields such as soft robotics, responsive aero- and hydrodynamic structures, and user-defined programmable materials, thereby further merging the digital and physical aspects of future engineering systems.

Materials and Methods

Injection molding and assembly: Part production and assembly details are shown in Figure S1. Parts were injection molded by Protolabs, a US-based CNC manufacturing service provider. To ensure low cost, parts were designed to be two-part moldable. While this is simple for the majority of the part, the inner-voxel tab and hole at 45 degrees required a custom designed opening, shown in Figure S1C. Parts were assembled with 3/32" diameter blind aluminum rivets, utilizing a pneumatic rivet gun. The voxel assembly process is shown in Figure S1D. Voxel to voxel joints used the same process, shown in Figure S1E. Metrics for assembly time and throughput are shown in Table S1.

Mechanical characterization: Small-scale tests to validate continuum behavior as shown in Figure 1 were performed on an Instron 4411 testing machine using a 5kN load cell. Lattice specimens for each type were tested in cubes of side length voxel count $n = 1, 2, 3$, and 4. Lattice tests were performed on an Instron 5985 testing machine using a 250 kN load cell. Specimens of a given lattice type were loaded to the same amount of relative strain, at an extension rate of 10 mm/min. Both machines use Bluehill 2 software for data acquisition. Video was recorded using a Nikon D3400 camera. Video was analyzed using Tracker, an open source video analysis and modeling tool (https://physlets.org/tracker/).

Numerical modeling: Fully meshed FEA simulations were used to check stress concentrations, but these typically incur higher computational costs Figures S5-6), and therefore were limited to under 10 voxels. A static stress analysis solver based on NASTRAN was used in Autodesk Fusion 360's built in simulation environment. Larger lattice models were simulated using the Frame3DD library, a freely available numerical solver implementing Timoshenko beam elements (http://frame3dd.sourceforge.net/) along with a python interface, PyFrame3DD (https://github.com/WISDEM/pyFrame3DD). For analysis of asymptotic behavior of large lattices Frame3DD was modified to incorporate sparse matrix math using CHOLMOD from the SuiteSparse library (https://github.com/DrTimothyAldenDavis/SuiteSparse). Python utilities were written to automate creating nodes, edges, faces and voxels, as well as applying loadings and boundary conditions using spatial rules (e.g. fixing the bottom of a lattice and applying forcing to the top nodes). These simulations were validated against a commercial software with comparable sparse matrix solving capabilities (Oasys GSA v9.0).

Acknowledgements

Funding: This work was supported by: NASA Cooperative Agreement #80NSSC19M0039, US Army Research Lab Cooperative Agreement #W911NF1920117, and CBA Consortia funding.

Competing interests: the authors cite no competing interests.

Author Contributions: BJ designed and produced parts, CC developed code to perform sparse matrix numerical modeling, FT performed numerical modeling using best-practice commercial packages, AP performed mechanical testing of lattice and subsystems, MO led lattice test specimen assembly, NG provided system architecture guidance.

Data availability: All data needed to evaluate the conclusions in the paper are present in the paper and/or the Supplementary Materials

References

1. L. Gibson, Cellular Solids: Structure and Properties (Cambridge University Press, 1999).
2. R. Lakes, Materials with structure hierarchy. Nature. 361, 511–515 (1993).
3. L. J. Gibson, M. F. Ashby, The Mechanics of Three-Dimensional Cellular Materials. Proc. R. Soc. A Math. Phys. Eng. Sci. (2006), doi:10.1098/rspa.1982.0088.
4. M. F. Ashby, The properties of foams and lattices. Philos. Trans. A. Math. Phys. Eng. Sci. 364, 15–30 (2006).
5. V. S. Deshpande, M. F. Ashby, N. a. Fleck, Foam topology: Bending versus stretching dominated architectures. Acta Mater. 49, 1035–1040 (2001).
6. T. A. Schaedler, A. J. Jacobsen, A. Torrents, A. E. Sorensen, J. Lian, J. R. Greer, L. Valdevit, W. B. Carter, Ultralight metallic microlattices. Science (80-.). 334, 962–965 (2011).
7. X. Zheng, H. Lee, T. H. Weisgraber, M. Shusteff, J. DeOtte, E. B. Duoss, J. D. Kuntz, M. M. Biener, Q. Ge, J. a Jackson, S. O. Kucheyev, N. X. Fang, C. M. Spadaccini, Ultralight, ultrastiff mechanical metamaterials. Science. 344, 1373–7 (2014).
8. X. Zheng, W. Smith, J. Jackson, B. Moran, H. Cui, D. Chen, J. Ye, N. Fang, N. Rodriguez, T. Weisgraber, C. M. Spadaccini, Multiscale metallic metamaterials. Nat. Mater. (2016), doi:10.1038/nmat4694.
9. L. R. Meza, S. Das, J. R. Greer, Strong , Lightweight and Recoverable Three - Dimensional Ceramic Nanolattices. Submitted. 345, 1322–1326 (2014).
10. J. B. Berger, H. N. G. Wadley, R. M. McMeeking, Mechanical metamaterials at the theoretical limit of isotropic elastic stiffness. Nature. 543, 533–537 (2017).
11. L. A. Shaw, F. Sun, C. M. Portela, R. I. Barranco, J. R. Greer, J. B. Hopkins, Computationally efficient design of directionally compliant metamaterials. Nat. Commun. (2019), doi:10.1038/s41467-018-08049-1.
12. Y. Jiang, Q. Wang, Highly-stretchable 3D-architected Mechanical Metamaterials. Sci. Rep. (2016), doi:10.1038/srep34147.
13. X. Ren, R. Das, P. Tran, T. D. Ngo, Y. M. Xie, Auxetic metamaterials and structures: A review. Smart Mater. Struct. (2018), , doi:10.1088/1361-665X/aaa61c.
14. F. Wang, Systematic design of 3D auxetic lattice materials with programmable Poisson's ratio for finite strains. J. Mech. Phys. Solids (2018), doi:10.1016/j.jmps.2018.01.013.
15. T. Frenzel, M. Kadic, M. Wegener, Three-dimensional mechanical metamaterials with a twist. Science (80-.). (2017), doi:10.1126/science.aao4640.
16. T. A. Schaedler, W. B. Carter, Architected Cellular Materials. Annu. Rev. Mater. Res. 46, 187–210 (2016).
17. A. R. Torrado, D. A. Roberson, Failure Analysis and Anisotropy Evaluation of 3D-Printed Tensile Test Specimens of Different Geometries and Print Raster Patterns. J. Fail. Anal. Prev. (2016), doi:10.1007/s11668-016-0067-4.

18. L. Bochmann, C. Bayley, M. Helu, R. Transchel, K. Wegener, D. Dornfeld, Understanding error generation in fused deposition modeling. Surf. Topogr. Metrol. Prop. (2015), doi:10.1088/2051-672X/3/1/014002.

19. L. Liu, P. Kamm, F. García-Moreno, J. Banhart, D. Pasini, Elastic and failure response of imperfect three-dimensional metallic lattices: the role of geometric defects induced by Selective Laser Melting. J. Mech. Phys. Solids (2017), doi:10.1016/j.jmps.2017.07.003.

20. C. E. Duty, V. Kunc, B. Compton, B. Post, D. Erdman, R. Smith, R. Lind, P. Lloyd, L. Love, Structure and mechanical behavior of Big Area Additive Manufacturing (BAAM) materials. Rapid Prototyp. J. 23, 181–189 (2017).

21. B. Khoshnevis, D. Hwang, K.-T. Yao, Z. Yah, Mega-scale fabrication by contour crafting. Int. J. Ind. Syst. Eng. (2006), doi:10.1504/IJISE.2006.009791.

22. X. Zhang, et al, Large-scale 3D printing by a team of mobile robots. Autom. Constr. (2018).

23. Nanoscribe GmbH, Nanoscribe Technology. nanoscribe.de/en/technology/ (2017).

24. Masterprint, (available at https://en.machinetools.camozzi.com/products/additive-manufacturing/all-products/masterprint.kl).

25. K. C. Cheung, N. Gershenfeld, Reversibly assembled cellular composite materials. Science. 341, 1219–21 (2013).

26. B. Jenett, D. Cellucci, C. Gregg, and K. C. Cheung, "Meso-scale digital materials: modular, reconfigurable, lattice-based structures," in Proceedings of the 2016 Manufacturing Science and Engineering Conference, 2016.

27. C. Gregg, J. Kim, K. Cheung, Ultra-Light and Scalable Composite Lattice Materials. Adv. Eng. Mater. (2018), doi:https://doi.org/10.1002/adem.201800213.

28. W. Chen, S. Watts, J. A. Jackson, W. L. Smith, D. A. Tortorelli, C. M. Spadaccini, Stiff isotropic lattices beyond the Maxwell criterion. Sci. Adv. (2019), doi:10.1126/sciadv.aaw1937.

29. N. Wang, Z. Zhang, X. Zhang, Stiffness analysis of corrugated flexure beam using stiffness matrix method. Proc. Inst. Mech. Eng. Part C J. Mech. Eng. Sci. (2019), doi:10.1177/0954406218772002.

30. V. Goga, "New phenomenological model for solid foams," in Computational Methods in Applied Sciences, 2011.31. L. L. Howell, S. P. Magleby, B. M. Olsen, Handbook of Compliant Mechanisms (2013).

32. P. Ziemke, T. Frenzel, M. Wegener, P. Gumbsch, Tailoring the characteristic length scale of 3D chiral mechanical metamaterials. Extrem. Mech. Lett. (2019), doi:10.1016/j.eml.2019.100553.

33. W. Langford, A. Ghassaei, and N. Gershenfeld, "Automated Assembly of Electronic Digital Materials," in ASME MSEC, 2016.

34. W. Langford and N. Gershenfeld, "A Discretely Assembled Walking Motor," in International Conference on Manipulation, Automation and Robotics at Small Scales, 2019.

35. N. Cramer, D. Cellucci, O. Formoso, C. Gregg, B. Jenett, J. Kim, M. Lendraitis, S. S. Swei, K. Trinh, G. Trinh, K. Cheung, Elastic Shape Morphing of Ultralight Structures by Programmable Assembly. Smart Mater. Struct. (2019).

36. Micropep, (available at http://micropep.com/).

37. E. . Andrews, G. Gioux, P. Onck, L. . Gibson, Size effects in ductile cellular solids. Part II: experimental results. Int. J. Mech. Sci. 43, 701–713 (2001).

38. M. S. Lake, E. C. Klang, Generation and comparison of globally isotropic space-filling truss structures. AIAA J. (1992), doi:10.2514/3.11078.

39. J. Christensen, M. Kadic, O. Kraft, M. Wegener, Vibrant times for mechanical metamaterials. MRS Commun. 5 (2015), pp. 453–462.

40. J. Bauer, L. R. Meza, T. A. Schaedler, R. Schwaiger, X. Zheng, L. Valdevit, Nanolattices: An Emerging Class of Mechanical Metamaterials. Adv. Mater. 29 (2017), , doi:10.1002/adma.201701850.

41. J. R. Greer, W. C. Oliver, W. D. Nix, Size dependence of mechanical properties of gold at the micron scale in the absence of strain gradients. Acta Mater. (2005), doi:10.1016/j.actamat.2004.12.031.

42. K. Finnegan, G. Kooistra, H. N. G. Wadley, V. S. Deshpande, The compressive response of carbon fiber composite pyramidal truss sandwich cores. Zeitschrift fuer Met. Res. Adv. Tech. (2007), doi:10.3139/146.101594.

43. L. Dong, H. Wadley, Shear response of carbon fiber composite octet-truss lattice structures. Compos. Part A Appl. Sci. Manuf. 81, 182–192 (2016).

44. L. Dong, H. Wadley, Mechanical properties of carbon fiber composite octet-truss lattice structures. Compos. Sci. Technol. (2015), doi:10.1016/j.compscitech.2015.09.022.

45. L. Dong, V. Deshpande, H. Wadley, Mechanical response of Ti-6Al-4V octet-truss lattice structures. Int. J. Solids Struct. (2015), doi:10.1016/j.ijsolstr.2015.02.020.

46. G. Trinh, D. Cellucci, B. Jenett, S. Nowak, S. Hu, M. O'Connor, G. Copplestone, K. Cheung, in IEEE Aerospace Conference Proceedings (2017).

47. B. Jenett, A. Abdel-Rahman, K. C. Cheung, N. Gershenfeld, Material-Robot System for Assembly of Discrete Cellular Structures. IEEE Robot. Autom. Lett. (2019), doi:doi: 10.1109/LRA.2019.2930486.

48. C. Coulais, E. Teomy, K. De Reus, Y. Shokef, M. Van Hecke, Combinatorial design of textured mechanical metamaterials. Nature (2016), doi:10.1038/nature18960.

49. G. W. Milton, A. V. Cherkaev, Which elasticity tensors are realizable? J. Eng. Mater. Technol. Trans. ASME (1995), doi:10.1115/1.2804743.

50. P. Patil, thesis, Massachusetts Institute of Technology (2019).

51. S. Kumar, S. Tan, L. Zheng, D. M. Kochmann, Inverse-designed spinodoid metamaterials. npj Comput. Mater. (2020), doi:10.1038/s41524-020-0341-6.

52. U. G. K. Wegst, Bending efficiency through property gradients in bamboo, palm, and wood-based composites. J. Mech. Behav. Biomed. Mater. (2011), doi:10.1016/j.jmbbm.2011.02.013.

53. Vahidifar, A., E. Esmizadeh, G. Naderi, and A. Varvani-Farahani. "Ratcheting response of nylon fiber reinforced natural rubber/styrene butadiene rubber composites under uniaxial stress cycles: Experimental studies." Fatigue & Fracture of Engineering Materials & Structures 41, no. 2 (2018): 348-357.

54. Harwood, J. A. C., and A. R. Payne. "Hysteresis and strength of rubbers." Journal of Applied Polymer Science 12, no. 4 (1968): 889-901.

55. SLM, (available at https://www.slm-solutions.com/).

56. J. Go, S. N. Schiffres, A. G. Stevens, A. J. Hart, Rate limits of additive manufacturing by fused filament fabrication and guidelines for high-throughput system design. Addit. Manuf. (2017), doi:10.1016/j.addma.2017.03.007.

57. T. Brajlih, B. Valentan, J. Balic, I. Drstvensek, Speed and accuracy evaluation of additive manufacturing machines. Rapid Prototyp. J. (2011), doi:10.1108/13552541111098644.

58. C. Schmidleithner, D. Kalaskar, in 3D Printing (IntechOpen, 2018), pp. 1–22.

59. L. L. N. Laboratories, Large-Area Projection MicroStereolithography, (available at https://ipo.llnl.gov/content/assets/docs/award-archive/lapusl.pdf).

Supplementary Materials

Video files:

Part geometry, molding, assembly

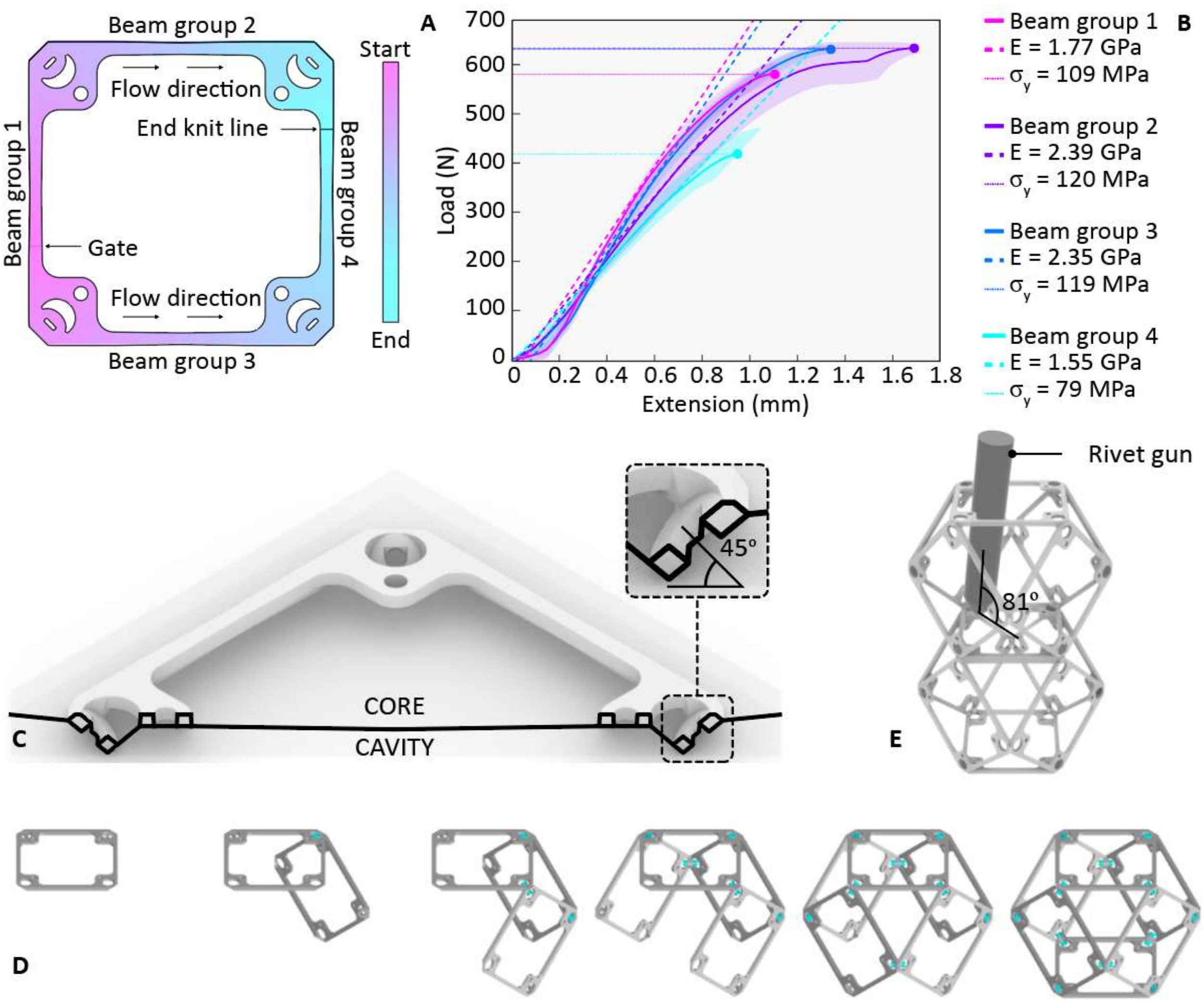

Figure S 1: Production of lattice by injection molding and assembly. *A) Injection molding gate layout and resulting material flow and knit line location, B) Characterization of different beam groups based on relative locations on part, C) Two part mold, with cavity below and core above, and a detailed view of the 45 degree angle hole, which is achieved by splitting the feature between core and cavity, D) Voxel assembly sequence. Faces are joined together one at a time, using rivets at the corners. A voxel consists of six faces and twelve rivets. E) Neighboring voxels are joined with the same method, rivet gun shown entering opposite face, at slight angle due to interference with inter-voxel joint node of entering face.*

We characterized the as-molded properties of the GFRP material, where the elastic modulus and yield strength vary based on the location of the gate and resulting knit lines. For injection molded FRP, fiber concentration reduces with distance from the gate. The highest concentration is around the gate, resulting in relatively high stiffness, but residual thermal and mechanical stress from the injection process cause a relatively lower yield strength. At the end of the flow, knit lines can result in around 50% yield strength reduction (*27*), in addition to reduced elastic modulus owing to distance from the gate. Therefore, controlling the location of these features is important. We want to avoid having the gate or knit line occur near the middle of the beam, where stress will be magnified during beam buckling induced strain. We also want to avoid having the end knit line occur on the inter- or inner-voxel nodes. Aside from operational stresses, during the voxel construction the outward force of the rivet expanding from actuation causes circumferential stress in the node area which can result in rupture along knit lines.

The resulting gate and knit line locations are shown for the rigid part type in Figure S1A, with contours indicating the flow location at increasing time steps. To characterize the range of as-molded material properties, specimens from each beam group were extracted from the faces and tested in uniaxial tension until failure, and the resulting elastic modulus and yield strength were calculated, as shown in Figure S1B. Our findings confirm several key aspects of part production. Beam group 1, which is closest to the gate, has high fiber content, thus a high elastic modulus, but has lower yield strength due to residual stress caused by gate proximity. Beam groups 2 and 3 have flows that move continuously from one end to the other, which promotes axial fiber alignment, giving a higher elastic modulus and yield strength. The last beam group has the lowest modulus, due to being at the end of the flow front, and the lowest strength, due to knit line proximity.

Scaling Study

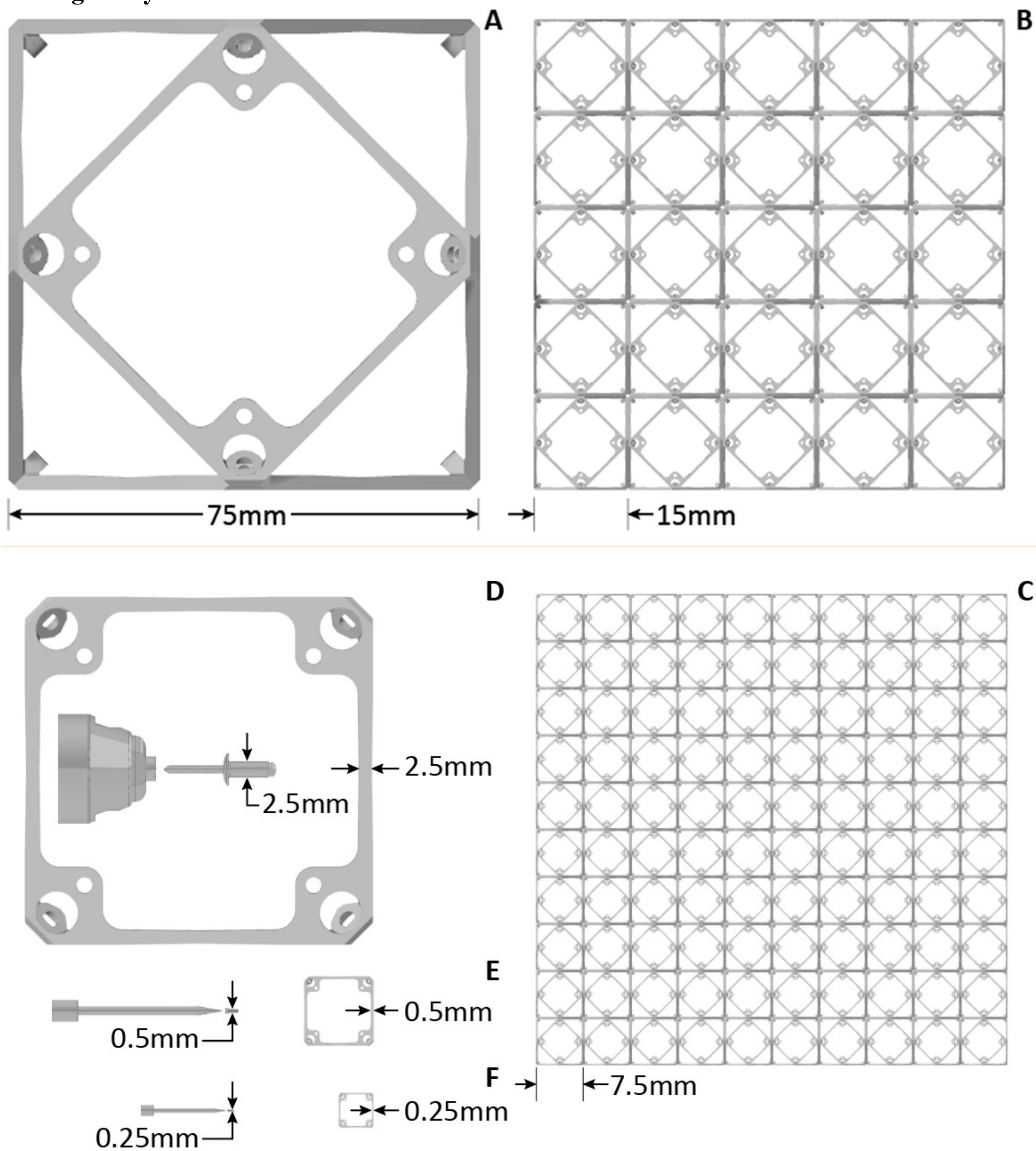

Figure S 2: Voxel scaling. *A) Current voxel with 75mm pitch, B) 5x shrink (20% original size) with 15mm pitch, C) x10 shrink (10% original size) with 7.5mm pitch, D) 75mm pitch face part with 2.5mm beam thickness and 2.5mm diameter rivet with rivet tool, E) 15mm pitch face part with 0.5mm beam thickness and 0.5mm diameter fastener (screwdriver shown for reference), F) 7.5mm pitch face part with 0.25mm beam thickness and 0.25mm diameter fastener with scaled screwdriver for reference.*

The scale of our system was originally driven by an application (see Figure S13). A 75mm lattice pitch was deemed appropriate in terms of spatial resolution (the higher the better) and number of parts (the fewer the better). But a 75mm unit cell is large compared to the majority of published lattice metamaterials, which typically have micrometer scale beam elements composing centimeter scale parts. One argument in favor of discrete assembly is the practicality: for tooling on the order of 10^3 USD and parts on the order of 10^0 USD, with commercially available fasteners and tools costing 10^2 USD, one can build large-scale mechanical metamaterials with no additional overhead. But if one wanted higher spatial resolution with a smaller unit cell, how well would the system presented here scale down? Here we can look at two critical aspects: part manufacturing and part joining.

Commercially available injection molding specifies minimum wall thickness of around 0.5mm, with some more specialized micro-molding services offering as thin as 0.15mm (*36*). Our parts have beam thickness of 2.5mm, so just looking at isometrically scaling the part down (which is sub-optimal, but useful for this exercise), we can get a part size shrink of 5x with typical commercial molding. Micro-molding can potentially provide up to x16 shrink; using a x10 shrink factor gives 0.25mm thick beams. So, while the cost model may become less favorable, micro-molding can produce lattice parts with 7.5mm pitch.

For joints, rivets do not scale down past 1/16” (1.35mm) diameter. The smallest commercially available screws tend to be 0000-xxx or M0.5, both with diameters of around 0.5mm. Based on the current design, scaling isometrically x5 would work. Fasteners with 0.25mm diameter for the x10 shrink may need to be custom made, which is a cost penalty. So the practical limit for this method is a 5x shrink (15mm pitch), but the technical limit is around 10x (7.5mm pitch). Smaller than this will likely require custom part and fastener manufacturing with processes such as subtractive laser milling commonly seen in MEMS fabrication (*50*). Clearly, at this scale, we do not come close to achieving the “size effects” shown at nanometer scale features, where effective properties such as strength exceed those of the constituent material (*40*) (*41*).

Discrete lattice load path analysis

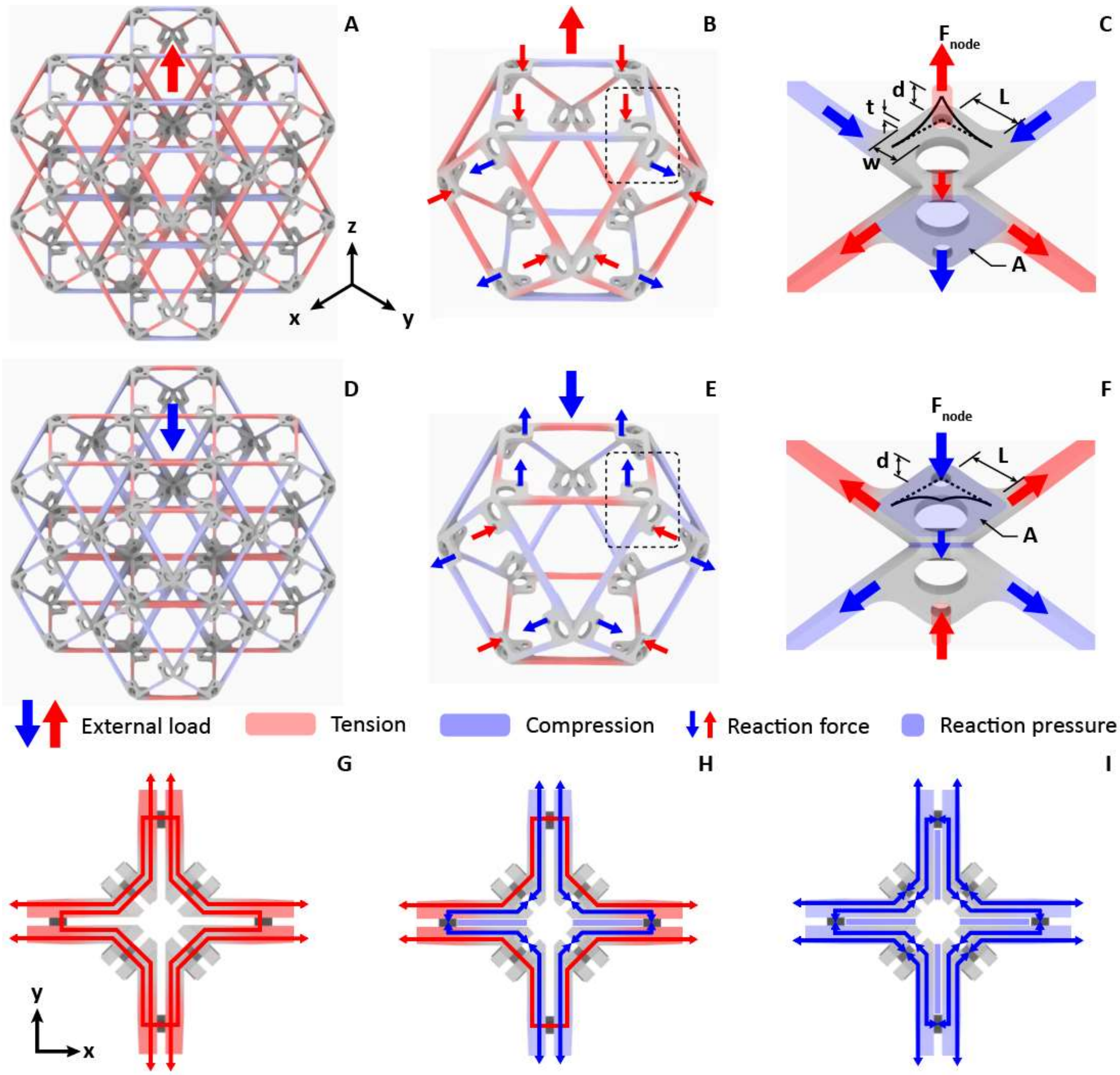

Figure S 3: Load paths in rigid Cuboct lattice. *A) 2x2x2 cube under uniaxial tension in Z direction, B) sample voxel under tension in Z direction, C) detail of corner joint showing internal load transfer, D) 2x2x2 cube under uniaxial compression in Z direction, E) sample voxel under compression in Z direction, F) detail of corner joint showing internal load transfer, G) illustration of cross-axis load transfer at joints, showing XZ and YZ planes in uniform tension, H) mixed compression and tension, and I) uniform compression.*

The rigid cuboct is taken as the base unit, which is used for describing system architecture such as critical dimensions and relative structural performance metrics. Figure S3A shows a 2x2x2 cube loaded in tension in the positive Z direction. We can observe that in-plane beams parallel to the loading direction (XY and YZ planes) go into tension, which results in the out of plane members (XY plane) go into compression. Assuming periodic boundary conditions, a single representative voxel is shown in Figure S3B, where external loading and reaction forces at outward facing nodes are shown. XY plane nodes logically go into tension on the top and bottom faces of the voxel. XZ and YZ faces have combined tension and compression reaction forces at the nodes, while all beams are in tension. Due to the construction employed, in-plane face loads are transferred through adjacent nodes to the outward face, which is normal to the load path direction, as shown in Figure S3C. At the junction of four, in-plane voxels, there are 3 possible load paths: all compression, all tension, or mixed tension and compression (Figure S3G-I). All compression is resolved through contact pressure of the node area, which helps in reducing the resulting pressure magnitude. All tension loads transfer from in plane beams, through inner-voxel joints, then through rivets which are parallel to the load path but fixtured to faces which are normal to the load path. Combined loads have overlapping, orthogonal load paths.

Hysteresis Characterization

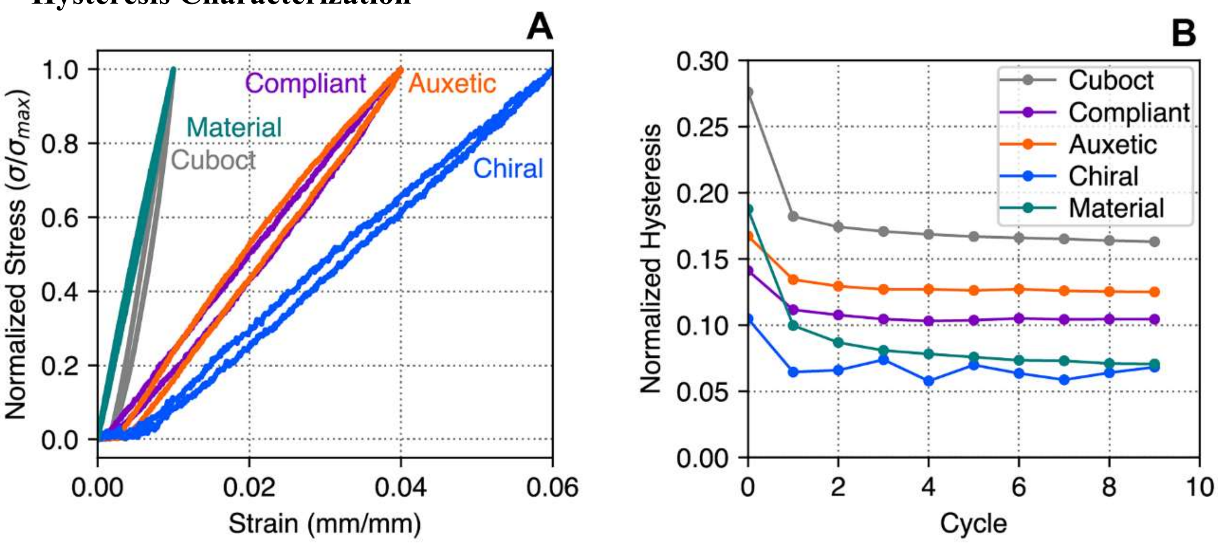

Figure S 4: Characterization of lattice hysteresis. *A) Single cycle hysteresis loops for lattice specimens (4x4x4 Cuboct, Compliant and Auxetic, 3x3x12 Chiral) as well as raw GFR Nylon material, B) History of hysteresis loop strain energy normalized by total strain energy for specimens in A*

While the voxel joints do not influence the static behavior of the lattice, they do introduce repeatable hysteresis through micro-slip at the riveted joints. Figure S4A shows representative hysteresis loops form a single loading-unloading cycle for the largest fabricated lattice samples and the raw lattice material, while Figure S4B shows hysteresis as a ratio of dissipated energy over loading strain energy for 10 complete cycles. All specimens exhibit an initial larger hysteresis loop, possibly due to Instron fixturing, before settling to consistent hysteresis levels in subsequent cycles. The cuboctahedral lattice, with the largest stresses at connection points, has the largest hysteresis magnitude, approximately twice that of the base material. This corresponds to matching the hysteresis of a rigid rubber at a fraction of a percent of the density (*53, 54*). The auxetic and compliant lattices have lower hysteresis, while the chiral sample displays no additional hysteresis compared to the bulk material. Hysteresis can be further reduced with preloaded joints (*27*).

Beam slenderness and relative density

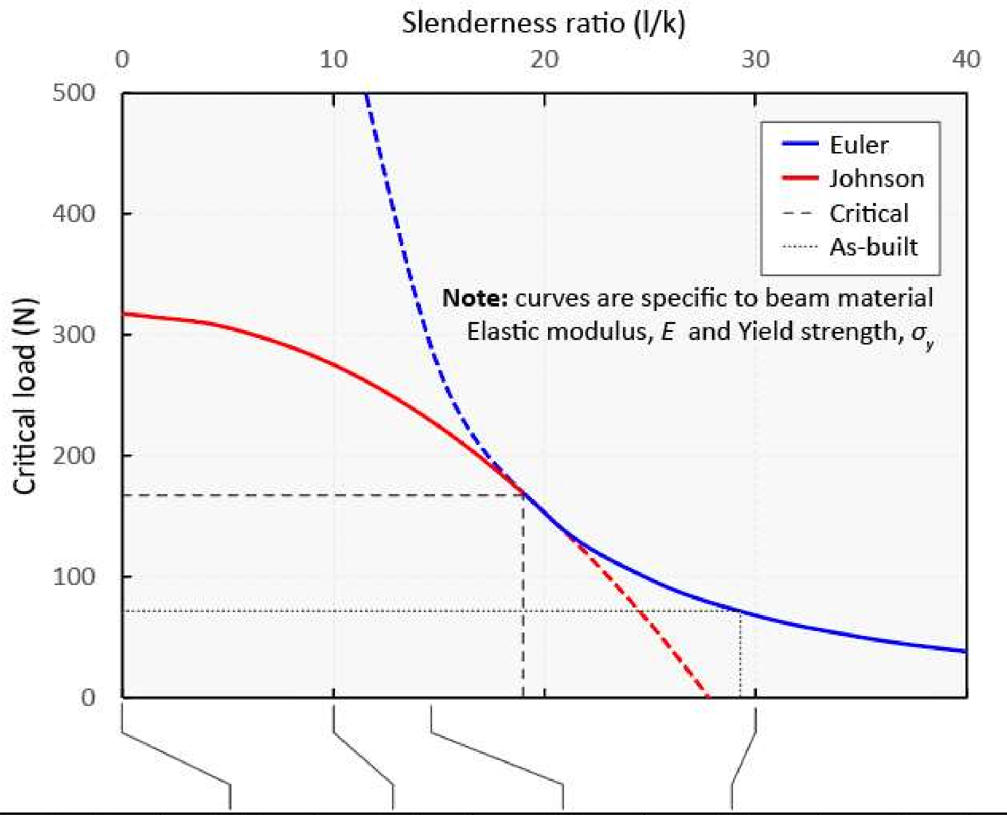

Relative Density	100%	30%	10%	5%	1%	0.5%
Beam slenderness ratio (l/k)	n/a	10:1	15:1	30:1	60:1	100:1

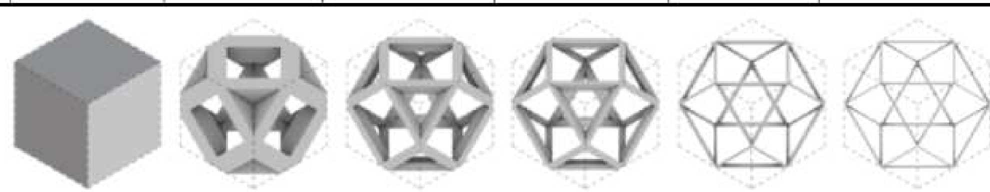

Figure S 5: Relationship between compression member slenderness ratio, failure mode, and resulting lattice relative density. *Beams above the critical slenderness ratio (l/k = 29.5) fail by elastic buckling, beams below fail by plastic buckling. Relative densities above 30% are invalid for cellular theory to apply.*

Here we discuss yield strength as the point at which initial beam failure occurs. The mechanism for this failure is important for understanding how the discrete lattice system behaves as a continuum lattice. As shown in Figure S 3, external loads are resolved internally as beam tension and compression. Beam tensile failure is determined by constituent material and beam cross sectional area, with the critical force $F_{cr} = \sigma_t * A$.

Beams in compression fail in different ways depending on their slenderness ratio, defined as effective length over radius of gyration, $\left(\frac{l}{k}\right) = L_{ef}\sqrt{A/I}$. This is used to describe three compression member types in terms of their failure modes: short, intermediate, and long. As cellular solid theory is only applicable at relative densities under 30%, we limit our analysis to beams with slenderness ratios above 4:1. For sparse Euler buckling is the elastic stability limit, and is applicable to long members, but as slenderness ratio goes to zero, Euler buckling predictions go to infinity. Therefore, the Johnson parabola curve considers material yield strain

(σ_y/E), the strain at which the material ceases to be linearly elastic, in calculating the inelastic stability limit. The transition between long and intermediate occurs at the critical slenderness ratio, which can be calculated using material and beam geometric properties (*40*).

Our material is a GFRP with an elastic modulus E = 2 GPa and yield strength σ_y = 107 MPa, and we can calculate critical slenderness using $\left(\frac{l}{k}\right)_{cr} = \sqrt{2\pi^2 E/\sigma_y}$ = 19.21. Based on our part geometry, we find our beam slenderness to be ~29.5. Therefore, our beams should fail based on Euler buckling at a critical load F_{cr} = 70N. Using the yield strength values from Figure S 7A, we can determine the experimental value for critical beam load by dividing the global peak load (7.8 kN) by the cross sectional voxel count (16), resulting in 487.5 N/voxel, 121.9 N/node, which is carried by two beams at 45 degree angles, giving a beam load of 86N.

Free body diagrams of each lattice type

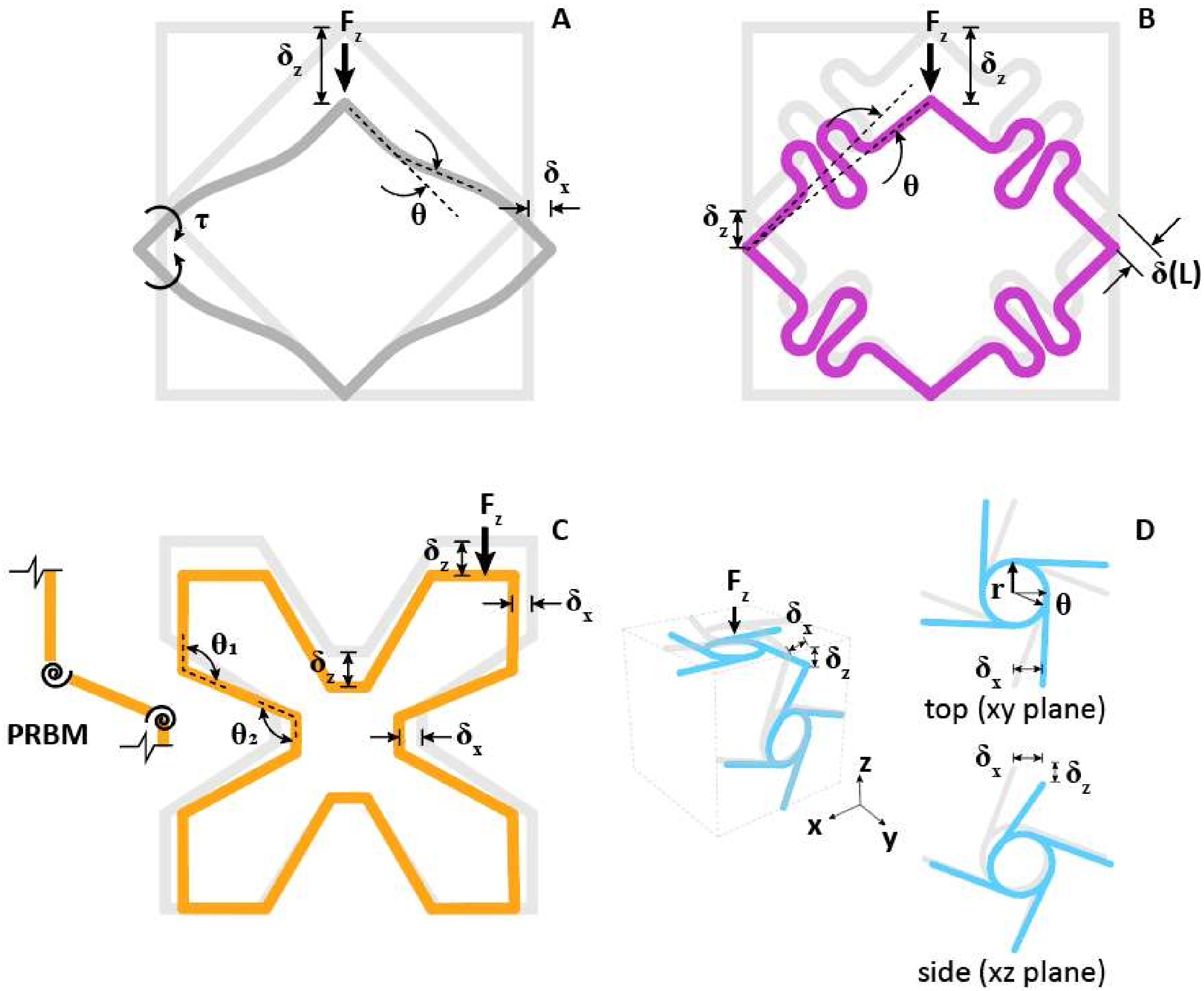

Figure S 6: Free body diagram of unit cell for each lattice type. *A) Rigid lattice type resolves external loads through axial member forces, in this case shown as compression and resulting member buckling, B) Compliant lattice type resolves external loads through axial shortening combined with a small amount of bending, producing little to no lateral reaction forces at nodes, C) Auxetic lattice type deforms through bending at the joints, and can be considered a pseudo rigid body model as shown to the side, D) Chiral lattice type deforms by bending and rotation in side faces, and nearly pure rotation in top face, thus producing chiral response.*

Boundary vs internal conditions with increasing voxel count

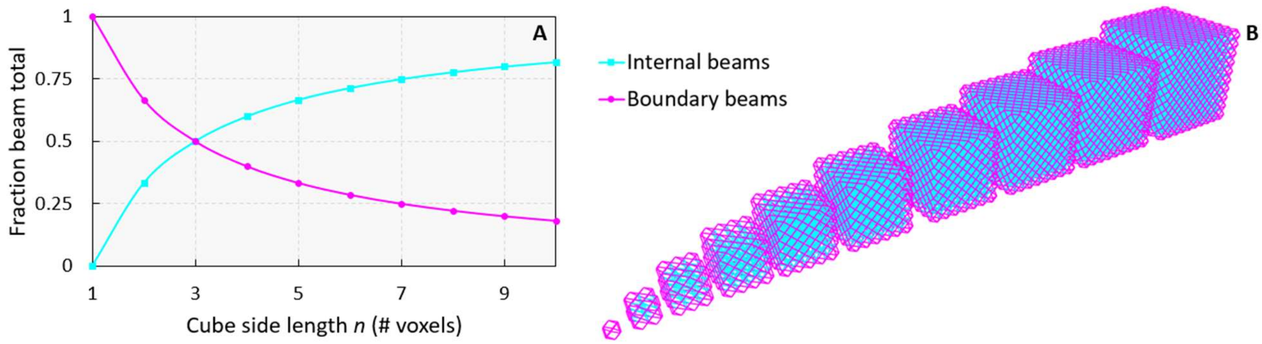

Figure S 7: Boundary vs internal conditions as a function of cube side length. *A) A single voxel is all boundary conditions, but this balances at n = 3, then continues increasing asymptotically for internal and decreasing asymptotically for boundary, B) Visualization of cube from n = 1 to n = 10.*

Numerical Modeling Comparison

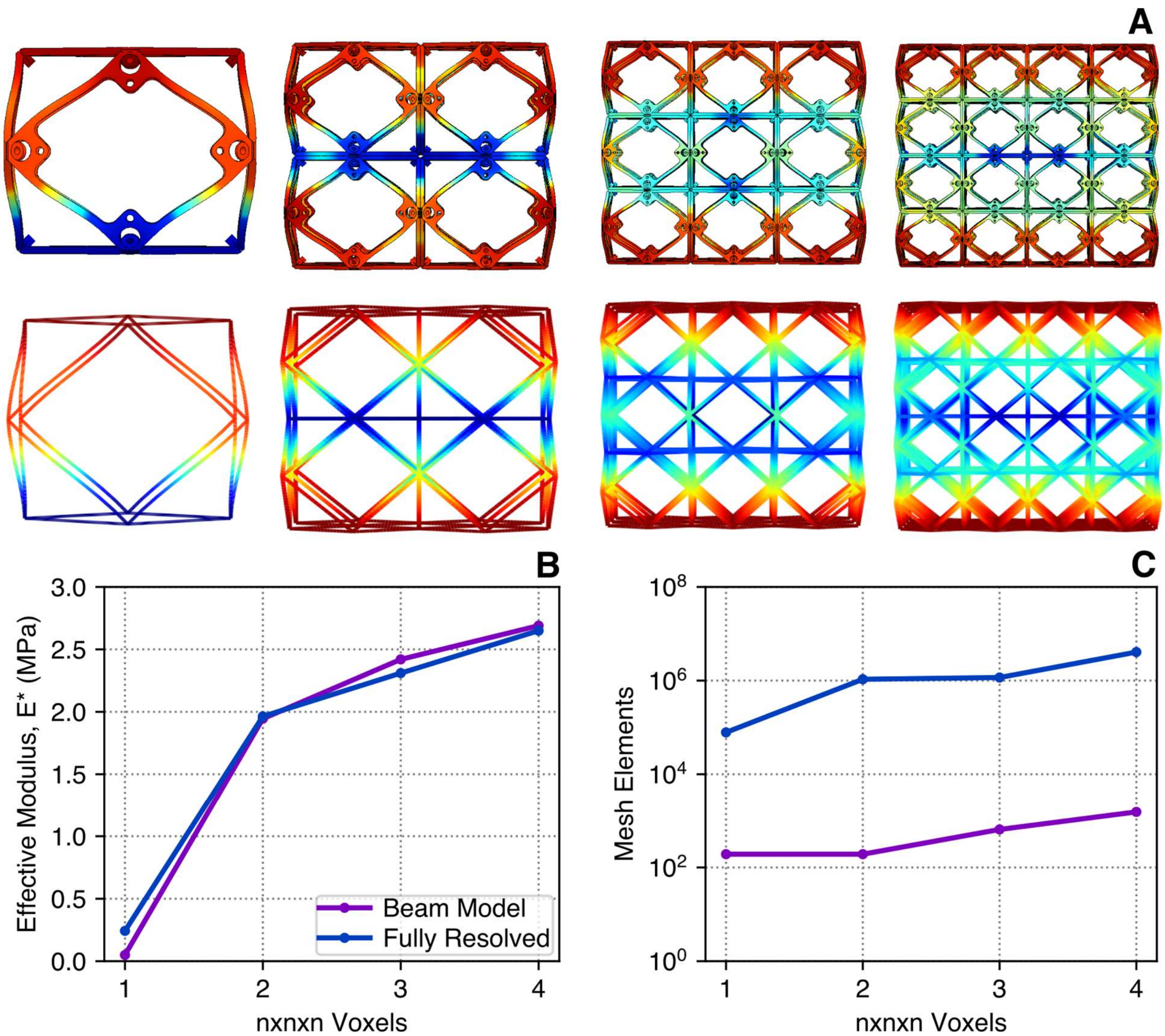

Figure S 8: Comparison of numerical models for rigid cuboct voxels. *A) Deformed cuboct lattices colored by displacement fully meshed FEA (top) and beam models (bottom), B) Comparison of effective modulus of beam and fully resolved FEA models, C) Number of elements for beam and fully meshed FEA models*

Here we compare fully meshed and beam FEA models. Figure S 8 A shows qualitative agreement between the fully meshed (top) and beam (bottom) models for uniform displacement boundary conditions. The effective moduli from the two models in Figure S 8 B show good agreement, with the largest relative error for a single voxel where the boundary conditions have a large effect on the voxel response. The number of elements needed to resolve the lattice samples is shown in Figure S 8 C. Fully meshed FEA results used adaptive mesh refinement to converge strain energy to within 95%, while beam mesh convergence studies are presented in Figure S 9. The fully meshed FEA requires approximately 3 orders of magnitude more elements than the corresponding beam model.

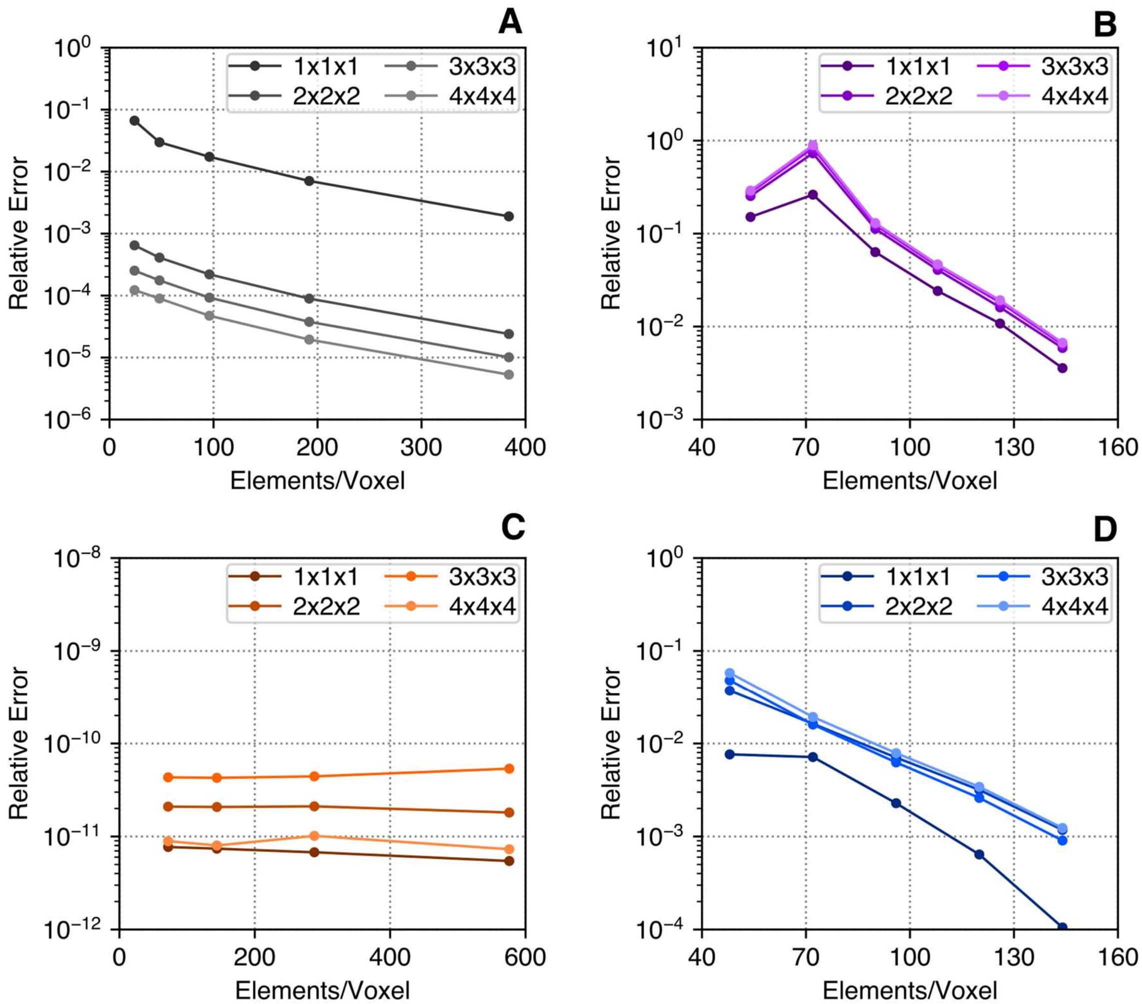

Figure S 9: Beam model mesh convergence studies. *A) Cuboctahedral lattice convergence of E*, B) Compliant lattice convergence of E*, C) Auxetic lattice convergence of Poisson ratio, D) Chiral lattice convergence of twist (degrees/% strain)*

Convergence studies for the four lattice types are shown in Figure S 9. The error is defined relative to a reference, highly refined result for the relevant quantity of interest for each lattice type: effective modulus, Poisson ratio, and twist for the cuboctahedral and compliant, auxetic, and chiral lattices respectively. All results presented in the main text are converged to within 1% of the reference solution. The cuboctahedral results for side length of 2 or greater are converged with just one beam element per edge, while the single voxel requires at least 8 elements per edge. This is related to the effect of boundary conditions and the increasingly extension dominated behavior of the cuboctahedral lattice as the number of cells increases. Convergence of the compliant and chiral voxels is dominated by increasing resolution of the curvilinear features present, while the Poisson's ratio of the auxetic voxels are converged to within model precision with just one element per beam.

Experimental results

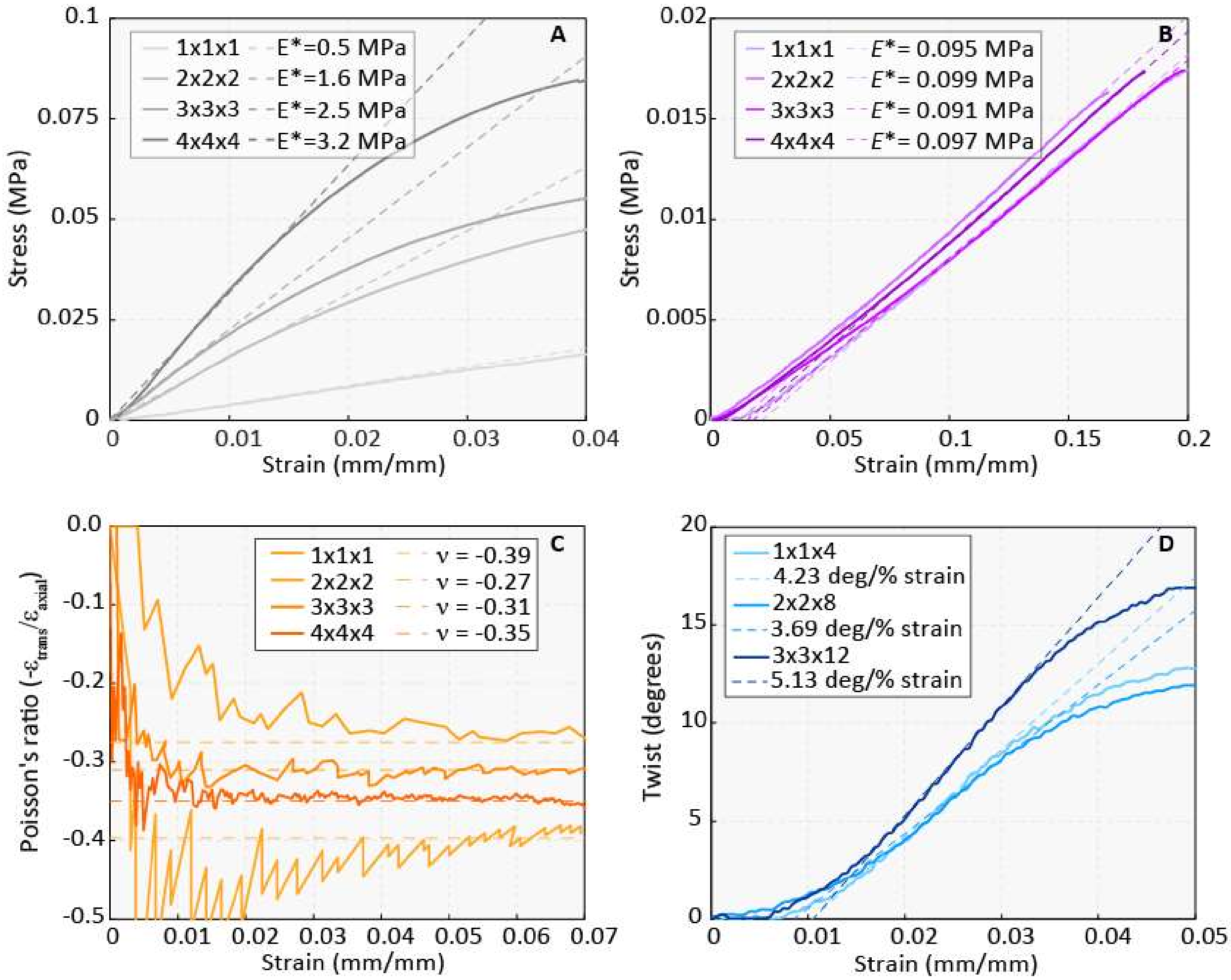

Figure S 10: Experimental results. *A) Rigid, B) Compliant, C) Auxetic, D) Chiral.*

Experimental lattice specimens

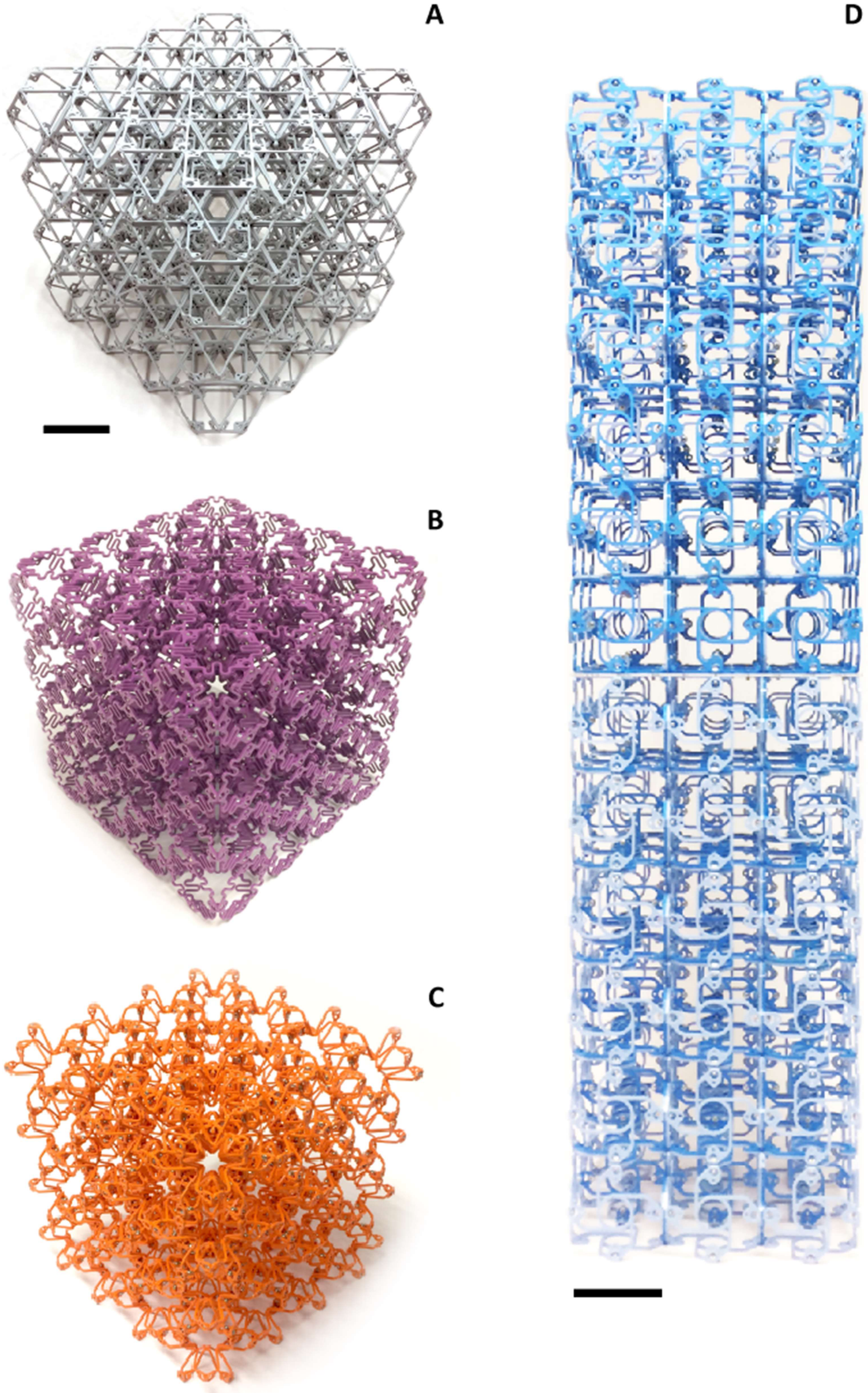

Figure S 11: As-built lattice specimens. *A) Rigid, B) Compliant, C) Auxetic, D) Chiral. Scale bar: 75mm.*

Macro-scale structural application

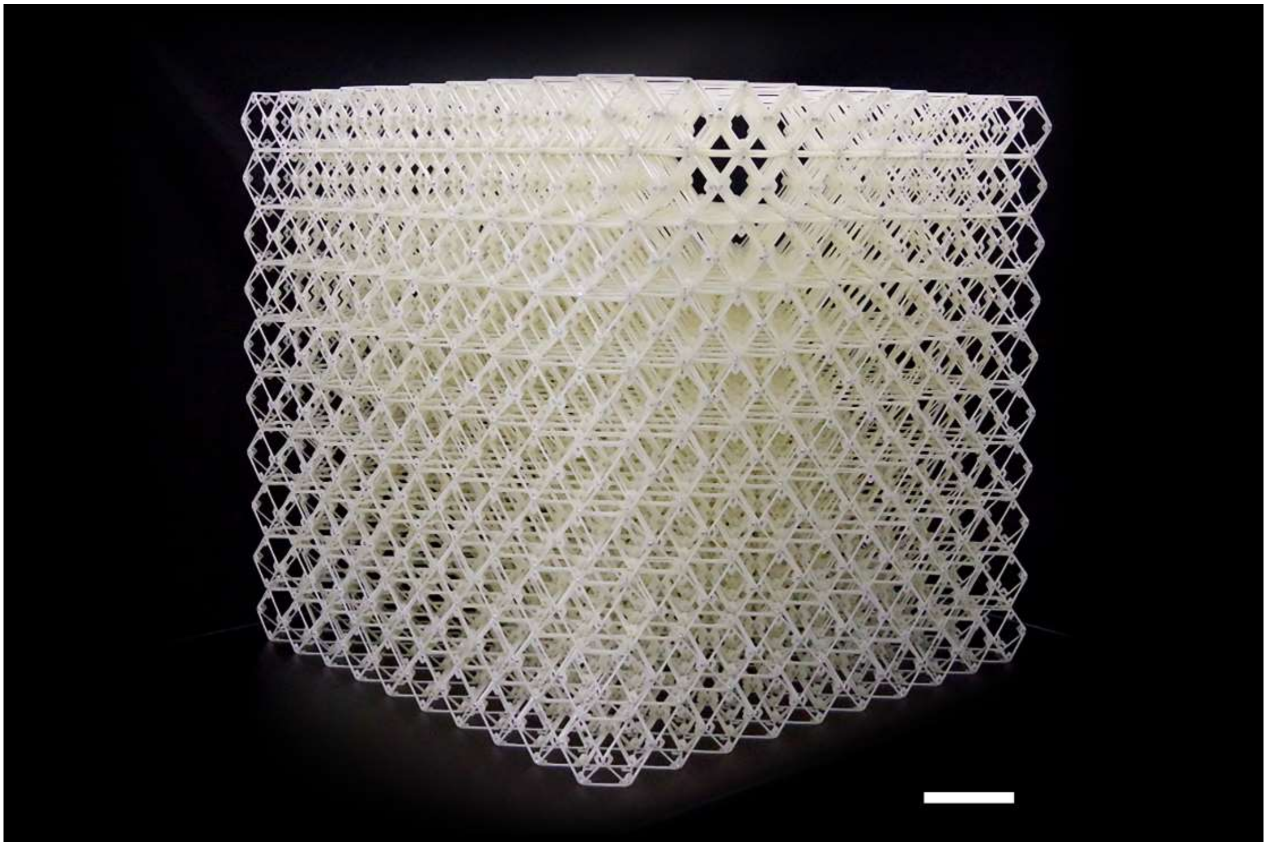

Figure S 12: 10x10x10 voxel cube. *Voxels are passively stacked, in preparation for assembly into cellular car frame shown in Figure S 11. Cube side length is 750mm. Scale bar: 100mm.*

Figure S 13: Large scale Application of discretely assembled mechanical metamaterial as a car frame. *A) Mass produced parts, B) Assembled layer, C) Completed frame without subsystems, D) Supermileage vehicle in operation. Scale bars A) 75mm, B) 225mm, C) 225mm, D) 150mm. Image credit: Kohshi Katoh, Toyota Motor Corporation.*

Table S1: Assembly metrics

Specimen cube voxel width *n*	**Total voxels**	**Total Rivets**	**Avg rivets/voxel**	**Time/ voxel (min)**	**Total time (min)**	**cm^3/hr**	**g/hr**
1	1	12	12	1.5	1.5	16,876	500
2	8	144	18	2.25	18	11,250	333
3	27	540	20	2.5	67.5	10,125	300
4	64	1344	21	2.625	168	9,643	285
5*	125	2700	21.6	2.7	337.5	9,375	277
10*	1000	22800	22.8	2.85	2850	8,882	263
N*	N^3	N^3*12 + [N^2*(3(N-1))]*4	24	3	3*N^3	8,440	250

* = projected (not built), Avg Rivet time = 7.5s, Voxel mass = 12.5g, Voxel vol = 422 cm^3

Table S2: Comparison between additive manufacturing and discrete assembly

Manufacturing Method	**Volume rate (cm^3/hr)**	**Mass rate g/hr**	**Machine/ setup cost**	**Part scale**
Selective laser melting (SLM) (*55*)	<170	<195	10^5-10^6	<1m
Fused deposition modeling (FDM) (*56*)	<60	<65	10^3-10^5	>1m
Polyjet (photopolymer) (*57*)	<80	<95	10^4-10^5	<1m
Stereolithography (SLA) (*58*)	<280	<340	10^4-10^5	<1m
Large area projection microstereolithography (LAPμSL) (*59*)	1.2	1.4	>10^6	<<1m
Discrete Assembly (this work)	≈5626	≈162	10^3	>1m